DESIGN AND DELIVERY OF NANOBODY FUSIONS AS IMMUNOTHERAPY FOR COVID19

A Thesis

submitted to

Indian Institute of Science Education and Research Pune in partial fulfilment of the requirements for the BS-MS Dual Degree Programme

by

Avadhoot Jadhav

Indian Institute of Science Education and Research, Pune

Dr. Homi Bhabha Road,

Pashan, Pune 411008, INDIA.

April, 2023

Under the guidance of

Supervisor: **Dr Hidde Ploegh**,

Senior Investigator at Boston Children's Hospital (Harvard Medical School)

May 2022 - Mar 2023

INDIAN INSTITUTE OF SCIENCE EDUCATION AND RESEARCH PUNE

Certificate

This is to certify that this dissertation entitled "**Design and delivery of nanobody fusions as immunotherapy for COVID19**" towards the partial fulfilment of the BS-MS dual degree programme at the Indian Institute of Science Education and Research, Pune represents study/work carried out by **Avadhoot Jadhav** at PCMM (Program in Cellular and Molecular Medicine) Department under the supervision of **Dr. Hidde Ploegh,** Senior Investigator at Boston Children's Hospital (Harvard Medical School), during the academic year 2022-2023.

Dr. Hidde Ploegh

Date: 7th April, 2023

TAC Committee:

Dr. Hidde Ploegh

Dr. M. S. Madhusudhan

This thesis is dedicated to my late grandfather, *Mr. Shankarao Aage*

Declaration

I hereby declare that the matter embodied in the report entitled “Design and delivery of nanobody fusions as immunotherapy for COVID19” are the results of the work carried out by me at PCMM (Program in Cellular and Molecular Medicine) Department, Boston Children’s Hospital (Harvard Medical School) and in affiliation with Indian Institute of Science Education and Research, Pune, under the supervision of Dr. Hidde Ploegh and Dr. M. S. Madhusudhan. The same has not been submitted elsewhere for any other degree.

Avadhoot Jadhav

Date: 7th April, 2023

Table of Contents

List of Abbreviations

BLI	Bio-layer interferometry
CDR	Complementarity-determining region
CF	Chemical fusion
ELISA	Enzyme-linked immunosorbent assay
FPLC	Fast protein liquid chromatorgraphy
GF	Genetic fusion
HDX-MS	Hydrogen–deuterium exchange mass spectrometry
hKappa VHH	Human kappa-light chain region targeting nanobody
mKappa VHH	Mouse kappa-light chain region targeting nanobody
NOTA	1,4,7-triazacyclononane-1,4,7-triacetic acid
PEG	Polyethylene glycol
PET	Positron emission tomography
RBD	Receptor binding domain of the SARS-CoV-2 spike protein
RMSD	Root mean square deviation
SDS-PAGE	Sodium dodecyl-sulfate polyacrylamide gel electrophoresis
SEC	Size-exclusion chromatography
SPR	Surface plasmon resonance

List of Tables

List of Figures

Main

Supplementary

Contributions

Contributor name	Contributor role
Dr. Hidde Ploegh, Dr. Xin Liu, Dr. M. S. Madhusudhan, Avadhoot Jadhav	Conceptualization Ideas
Dr. Hidde Ploegh, Dr. Xin Liu, Avadhoot Jadhav	Methodology
Avadhoot Jadhav, Tejashree Kanitkar	Software
Avadhoot Jadhav	Validation
Avadhoot Jadhav	Formal analysis
Avadhoot Jadhav, Dr. Xin Liu, Claire Carpenet	Investigation
Dr. Xin Liu, Dr. Ryan Alexander, Dr. Novalia Pishesha, Tejashree Kanitkar	Resources
Avadhoot Jadhav	Data Curation
Avadhoot Jadhav	Writing - original draft preparation
Dr. Hidde Ploegh	Writing - review and editing
Avadhoot Jadhav	Visualization
Dr. Hidde Ploegh, Dr. Xin Liu	Supervision
Avadhoot Jadhav	Project administration
Avadhoot Jadhav, Dr. Hidde Pleogh	Funding acquisition

Abstract

SARS-CoV-2, the virus responsible for the COVID-19 pandemic, has infected millions of lives worldwide, causing a significant number of deaths. Despite the development of several drugs and vaccines, the emergence of new variants creates the need for alternative therapeutic approaches. In this study, we demonstrate the potential of a nanobody binder, E11, to target a conserved site and bind to most variants of SARS-CoV-2 with nanomolar binding affinity. We also explore the use of novel nanobody fusions with E11, synthesized both genetically and chemically, to specifically bind to SARS-CoV spike-expressing cells with high affinity and recruit polyclonal IgGs. Our results show that these fusions can effectively activate effector functions, including Complement Dependent Cytotoxicity, of both mouse and human polyclonal IgGs against SARS-CoV-2 infected cells. Moreover, our fusions demonstrate their ability to target almost all currently known variants SARS-CoV-2. To our knowledge, this is the first nanobody-nanobody fusion to show selective elimination of SAR-CoV-2 virus-infected cells in vitro at nanomolar range. Our findings suggest that E11-based nanobody fusions may serve as a promising therapeutic approach against COVID-19, especially in the context of emerging variants.

Acknowledgments

I am deeply indebted to the following individuals whose invaluable contributions have helped me develop this project successfully.

First and foremost, I express my gratitude to Xin Liu for his exceptional guidance and support in conducting the experiments. His insights and expertise have been instrumental in shaping this project.

I am also grateful to Tejashree Kanitkar for her unwavering support and guidance in the computational aspects of this project. Her dedication and expertise have been crucial in achieving the desired results.

I would like to extend special thanks to several individuals who have played a crucial role in this project. Ryan Alexander has been an invaluable contributor to the mice work and ADCC experiments, and his unwavering belief in me has been a constant source of encouragement. Novalia Pishesha's provision of necessary resources has been crucial in facilitating the experimental work, while Pavana Suresh's guidance in basic wet lab techniques has been extremely helpful. Additionally, Thomas (both M. and B.) and Elisha's advice on TC techniques has been instrumental in preventing cell contaminations. Thanks to Claire Carpenet for her help with PET imaging. I am also indebted to other members of the Ploegh lab – Lotte, Cameille, Himadri, Eugene and Jin for their invaluable suggestions and constructive criticism throughout the project.

I also extend my gratitude to my colleagues Anouk, Richard, Katherine, Manpreet, Priscilla, Isabelle, Mannon, Mirna, Francisa, and Nanette for their cooperation and encouragement. Their moral support has been invaluable, especially during the challenging times when experiments failed. I am also grateful to Simona Stella and Robert Miller for their administrative support and assistance, even beyond the lab.

I would like to express my appreciation to my family and friends, who have been a constant source of love and support throughout this journey. Special thanks go out to Anant, Farah, Ayushi, Kian, Dhruv, Shweta, Sid, Deepak, Himanshu, Niko, my Frisbee Ultimate Team, and the 50 Year's team, whose encouragement and belief in me have been crucial in helping me navigate the ups and downs of this journey.

I must acknowledge that this project would not have been possible without the two most important people. I am extremely grateful to Dr. M.S. Madhusudhan for his unfaltering support and belief in me throughout this journey. His expertise and guidance, both in scientific and non-scientific aspects have been crucial in inspiring me and enabling me to achieve my goals.

I want to give a big thanks to Dr. Hidde Ploegh. Not only did he provide me with the incredible opportunity to dive headfirst into wet lab work, but he did so knowing full well that I had about as much experience with a pipette as a toddler does with chopsticks (i.e., not much). I'm pretty sure he had a good chuckle watching me fumble around in the lab at first, but thanks to his unwavering support and scientific expertise, I managed to avoid burning the place down and actually accomplish something pretty cool. So, from the bottom of my heart, thank you, Dr. Ploegh, for believing in me and giving me the chance to become a real-life wetlab wizard!

Finally, I extend my thanks to the New Science team- Sasha Targ for her project feedback and ideas, Niko McCarty for his advice in reading and writing, and Alexey Guzey for funding this project. Their contributions have been crucial in shaping the success of this project.

Chapter 1 Introduction

1.1 COVID19: A major health crisis

The COVID-19 pandemic has now lasted for more than three years. For many pathogens, including this virus, drug resistance and immune evasion continue to rise. Evidence suggests reduction in vaccine effectiveness against many of the 'newer' variants, such as Alpha (B.1.1.7), Beta (B.1.351), Gamma (P.1), Delta (B.1.617.1) and Omicron (B.1.1.529)[1]. Many of these have been associated with increasing numbers of infections and disease-rebound cases, both among vaccinated and unvaccinated individuals[2–4].

As of January 2023, Omicron and its subvariants — especially the Omicron lineages XBB and BQ.1.1 — have been identified as the predominant SARS-CoV-2 strains that are causing new epidemic waves in the world. Recent reports show significant enhancements in the transmissibility and/or immune evasion abilities of these subvariants. As a consequence, the efficacies of existing vaccines have been questioned[5–7]. Similarly, viruses have begun to develop resistance against antiviral drugs that target a single location, such as Paxlovid and Molnupiravir, due to changes in the epitope structure of the viral protein[8,9].

Monoclonal antibodies (mAbs) and antibody derivatives are a promising class of therapeutics to control infection by preventing viral entry into cells. Full-size IgG proteins have been created in a chimeric or humanized format to make mAb therapies[10]. Many FDA-approved neutralizing monoclonal antibodies (mAbs), such as bamlanivimab (BAM) and etesevimab (ETE), have also proved effective in passive immunization by targeting the SARS-CoV-2 spike protein and disrupting the virus entry[11,12]. However, the emergence of newer variants has significantly reduced their efficacy against them. As of December 2022, reports from the Centers for Disease Control and Prevention (CDC) indicate that several Omicron subvariants are resistant to the currently available mAbs[13]. Currently, there are no recommended monoclonal antibodies for the treatment of COVID-19[14]. Although mAbs are potential drug candidates, they are expensive to produce, susceptible to temperature-dependent denaturation, and may lose efficacy with even minor changes in epitope structure[15,16]. Therefore, the development of broader and more effective therapies is necessary to address the pressing global concern of emerging variants.

1.2 A protein fusion based therapy

A fusion protein-based approach overcomes many of the shortcomings posed by monoclonal antibodies, and offers a possible solution to deal with the problem of emerging variants. Proteins are modular in nature and are composed of domains, which are independently folded regions within a protein. Such modularity enables functional protein domains to be joined together synthetically or genetically, with the goal of altering their function to modulate the immune system. The therapeutic efficacy of a protein of such design can be enhanced by choosing fusion partners that selectively target particular cell types or receptors[17].

Nanobodies have emerged as a versatile source for generating fusion constructs due to their unique properties. They are derived from the variable domain of heavy-chain-only antibodies, which are found in the immune systems of camels, llamas, and alpacas[18]. Nanobodies consist of a single domain and are ~10x smaller than traditional antibodies. They can be easily produced in high yields using bacterial expression systems[19,20]. Nanobodies bind to cognate targets with high specificity and affinity, which makes them efficient in detecting and neutralizing disease-causing antigens[21]. Moreover, nanobodies have high thermostability, which allows them to tolerate harsh conditions, such as high temperatures or extreme pH values, thereby making them resistant to denaturation and degradation[22]. Nanobodies have biochemical properties that make them suitable for a wide range of biotechnological and biomedical applications[23].

1.3 Strategy in a nutshell

We lay out a strategy to design and deliver nanobody fusion proteins that can target a specific protein — such as the SARS-CoV-2 spike — at conserved sites on its surface. Once bound to the virus, these fusion proteins recruit components of the immune system to selectively eliminate the virus-infected cells. In my thesis, I describe our strategy, focusing on using the SARS-CoV-2 spike antigen as an example.

My fusions consist of two components: A binder and a recruiter. I first identify protein binders that could target most if not all of the SARS-CoV-2 spike variants. I then fuse these binders to a recruiter — a specific nanobody that attracts polyclonal immunoglobulins — to generate an immune response against the virus infected cells.

To find a spike protein binding partner, I use two parallel approaches- computational design of peptide binders and a literature search for a known conserved binder. I use a computational algorithm to design peptide binders that target the spike protein at various distinct sites. The algorithm designs these peptides using CDRH3 (Complementarity Determining Region Heavy cha3) paratope mimicry, based on existing data from solved antibody-SARS-CoV-2 spike protein co-crystal structures. In

parallel, I review existing literature to search for a spike-binding nanobody and perform structural analysis to identify a conserved binder.

The spike protein binders are then conjugated to a nanobody that binds immunoglobulin (Ig) light chains, regardless of specificity or isotype of the heavy chain, to create novel genetic and chemical fusion therapeutics. In my thesis, I show that:

1. Our identified binder (E11) targets a conserved site and binds to most variants of SARS-CoV-2 with nanomolar binding affinity
2. Novel nanobody fusions with E11 — both genetic and chemical — can bind to SARS- CoV-spike expressing cells with nanomolar binding affinity and recruit polyclonal IgGs.
3. These fusions can activate effector functions (such as CDC) of both mouse as well as the human polyclonal IgGs.
4. Attempts at identifying peptides that resemble paratopes capable of binding to SARS-CoV-2 were not successful.

A brief video explains the project in greater detail

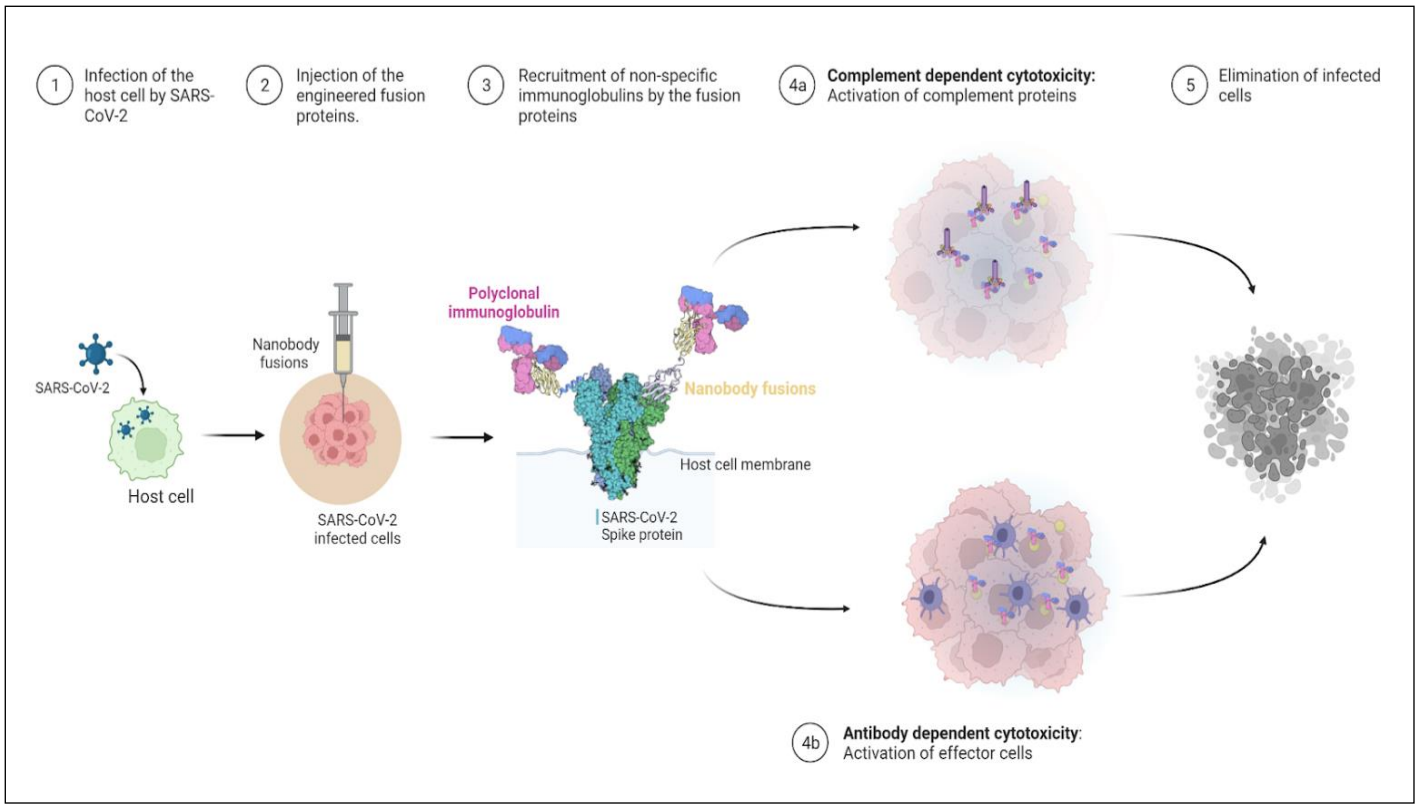

Figure 1. Schematic representation of the mechanism of action of nanobody fusions as a therapeutic strategy against viral infection. (1) The virus infects the host cells. (2) Nanobody fusions are administered as therapy. (3) The fusions specifically bind to the spike protein expressed on the infected cell surface and recruit polyclonal IgGs. (4a) This leads to the activation of complement-dependent cytotoxicity (CDC) and (4b) antibody-dependent cell-mediated cytotoxicity (ADCC). (5) The infected cells are eliminated, thus preventing further viral spread.

Things to ponder:

"In 2015, an article published in Nature estimated that 800,000,000 USD is wasted annually on nonspecific antibodies[24]*. Imagine if we could harness the effector functions of these antibodies regardless of their specificities."*

Chapter 2 Results and Discussion

2.1 Identification of spike binders

In this section, we present two approaches to identify SARS-COV-2 spike binders: computational design and a literature search. In addition, we describe the structural analysis used to identify conserved binders.

2.1.1 Computational design of peptide binders

Small peptides derived from the antigen-binding site or paratope have been recognized as effective downsized binding partners. Antibodies have a Y-shaped architecture, made up of two identical light and heavy chains, each with several domains. The variable light and heavy chain domains together form the Fv fragment. The three hypervariable loops present in each Fv fragment are called the Complementarity Determining Regions (CDRs). These loops are the primary determinants of antigen recognition. Over the past decade, the rational design of peptides using mimicry of the monoclonal antibody (mAb) paratope, primarily determined by the CDRs, has been studied as a successful strategy for developing therapeutics. For instance, *Levi et al.* derived a linear peptide derived from the CDRH3 loop sequence of a gp120-targeting monoclonal antibody and showed that it suceessfully inhibited replication of HIV-1 virus (IC_{50} = 274 μM)[25].

Peptides are much smaller in size (1-2 kDa) than most biologicals. This significantly reduces their production costs. This also contributes to low immunogenicity and toxicity, making them suitable for clinical use. We speculate that a mixture of peptides, each recognizing a different epitope, would be far more challenging to escape from by mutation, while resistance is often acquired for a single drug molecule[26,27].

We developed a computational algorithm, called PepLiDe (Peptide Library Designer), that generates a library of peptide binders for a given target protein, using known crystallographic structures of protein targets complexed with an antibody. The PepLide algorithm is currently being generalized to target any arbitrary protein target. Details about the algorithm will be published in the near future.

Briefly, for the present case, the algorithm first identifies the epitopes on the spike protein that have multiple binding partners (antibodies). I hypothesize that these regions may serve as effective binding sites for peptides to bind. Using this structural information, the algorithm produces peptide sequences that mimic the interacting segments of the binding partners, such that they leverage most of these

interactions and are predicted to target these crucial sites effectively. **The design makes the assumption that the linear peptides retain the conformation seen in the bound structure as its lowest energy state in solution when isolated.** I will conclude below that this assumption may not be justified.

Starting with 200 spike-bound antibody crystal structures, we generated a library of 276 unique peptides considered capable of binding to the spike protein. These peptides were then assessed in various scoring schemes such as FOLDX and PIZSA to improve confidence in their abilities to bind the intended target[28,29]. Six top-ranking peptides were selected based on their calculated binding energies for the spike protein. The stability of these peptide-protein complexes were further validated using MD simulations.

We speculated that a mixture of these peptides might effectively bind to most variants of the spike structure, as they target distinct sites and have been derived from a large dataset of all the available crystal structures. The six candidate peptides identified and filtered using the computational algorithm are listed in **Table S1**.

2.1.2 E11: A known nanobody binder from the literature

Nanobodies are effective at targeting conserved epitopes that are deeply buried, which are often inaccessible to larger antibodies. This is due to the nanobody's small size and the fact that they do not require the presence of a second variable domain for binding. It allows them to easily navigate through narrow spaces and penetrate areas that are less accessible to intact immunoglobulins[20]. Hence, we performed a literature search for a nanobody binder that could target conserved regions of the SARS-CoV-2 spike protein.

In 2021, *Hanke et al*. applied a novel multivariate mining approach of alpaca immune repertoire to identify potential nanobodies that could efficiently neutralize the virus. They found 11 potential candidates - E4, C7, E2, G6, C11, E11, F12, G1, F1, G2, D4 and D9. After evaluating these nanomolar binders, we selected E11 for further examination, based on a range of favorable characteristics. First, E11 exhibited high binding affinity, as evidenced by its K_d value of 5.3×10^{-11}, based on SPR (Surface Plasmon Resonance) binding kinetics analysis. E11 did not impede the binding of fluorescently labelled spike protein to HEK293-ACE2 target cells in a competitive binding assay performed using flow cytometry, suggesting that it may still bind to the spike protein even if mutations occur in the ACE2 binding epitope. While E11 only displayed moderate levels of neutralization activity against the SARS-CoV-2 Wuhan variant (IC_{50} = 0.1-1 µg/ml) in a pseudotyped lentivirus assay, it demonstrated cross-neutralization activity against the SARS-CoV-2 Wuhan variant (2019), SARS-CoV-1, and a Beta variant, suggesting it may be effective against the latest Omicron sub-variants[30]. We speculate that our fusion strategy would enhance the capacity of E11 to eliminate

infected cells. Finally, our structural analysis predicted that E11 in principle should bind to all known variants of SARS-CoV-2 – (details in the next section).

2.1.3 Structural analysis of spike binders

RBD is the primary site at which mutations accumulate for several variants, including Alpha (B.1.1.7), Beta (B.1.351), Gamma (P.1), Delta (B.1.617.2), Omicron (B.1.1.529) and subvariants. These mutations are the major drivers of immune evasion. They enhance transmissibility of the SARS-CoV-2 variants[31–33]. We identified the conserved areas on the RBD in order to determine whether our binders specifically targeted a conserved epitope on the SARS-CoV-2 spike protein. To do so, we identified the "Mutation hotspot of RBD" by mapping the ensemble of mutations corresponding to the aforementioned variants on the RBD structure (**Figure 2H**). Areas outside mutation hotspots were found as conserved sites.

Peptides whose location of interaction fell outside the mutation hotspot region were considered as conserved binders. **Figure 2** shows the epitopes on the RBD that interact with the 7 peptide candidates which were identified by zoning at a distance cutoff of 5 Å. Peptide 7m7w_S_C_752 showed no overlap of interacting residues with residues in the mutation hotspot, implying that it potentially targeted a conserved region on the RBD. Peptides 7l0n_R_A_312 and 7kmg_C_A_47 showed an overlap with the mutation hotspot of 2 and 3 residues, respectively **(Table S1).** These peptides were subjected to further computational assessments of binding affinity, discussed in later sections.

The published Hydrogen Deuterium Exchange Mass Spectrometry (HDX-MS) data indicated that E11 interacts with residues 375 to 387 and 423-431 on the RBD[30]. We found that only 2 residue sites (375 and 376) overlapped with the mutation hotspot, as shown in **Figure 4A.** This analysis strongly suggested that binding of E11 should not be affected by the mutations. We next attempted to confirm our hypothesis experimentally as described in the following sections.

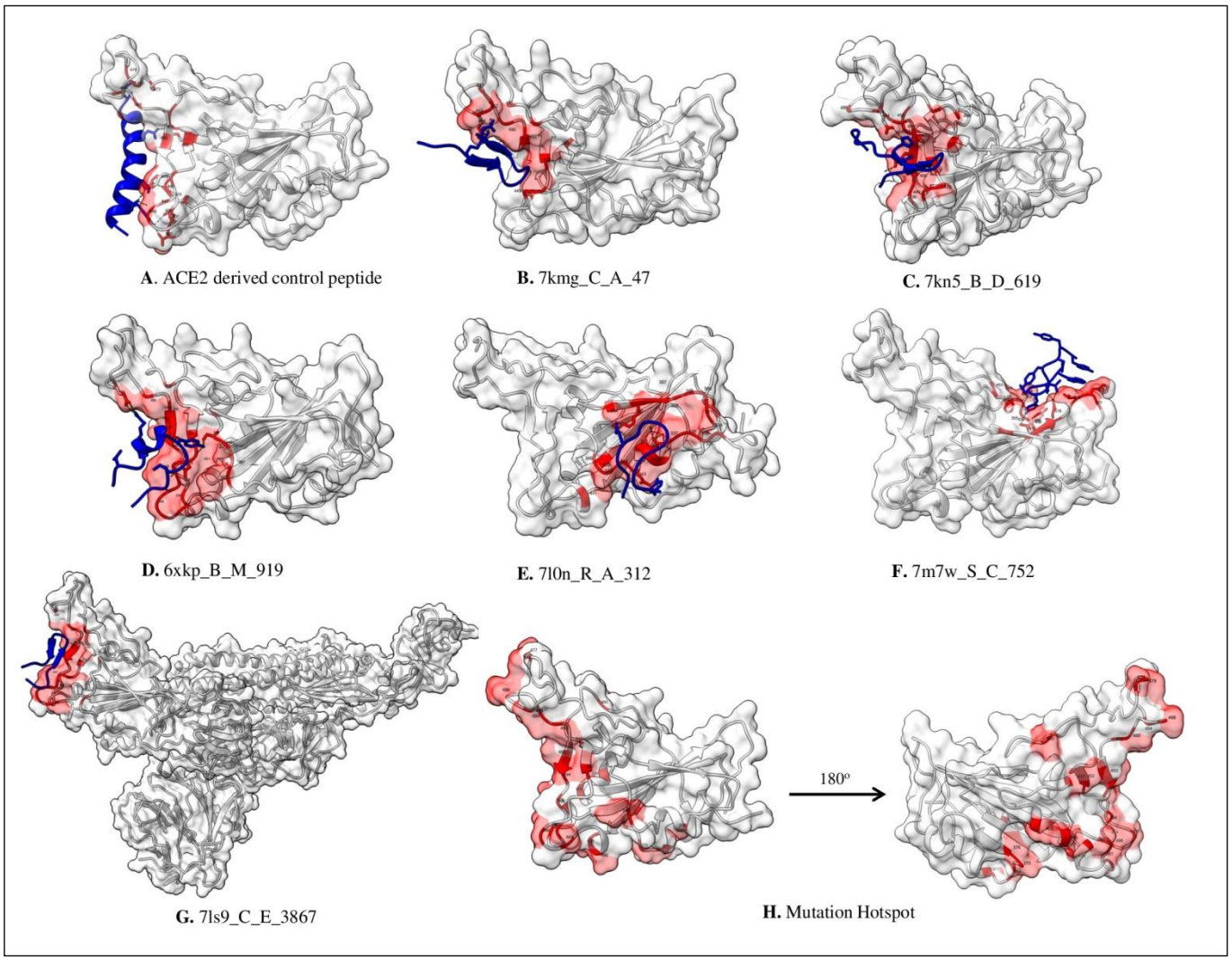

Figure 2. Spike protein binding locations on RBD and mutation hotspot region. Residues that interacted with any of the residues in the peptide were colored red. The binding locations of peptides, including the ACE-2 derived control peptide, 7kmg_C_A_47, 7kn5_B_D_619, 6xkp_B_M_919, 7l0n_R_A_312, 7m7w_S_c_752, and 7ls9_C_E_3867, are depicted in panels (A) to (G). The mutation hotspot region on the RBD surface is highlighted in red in panel (H).

2.2 Synthesis and functionalization

Functionalization involves the attachment of additional functional groups to a molecule of interest — nanobodies in our case — to impart specific properties or functions, such as targeting, imaging, or drug delivery. Here, we describe three methods that we used for functionalizing nanobodies for downstream applications:

Genetic fusion: Nanobodies can be fused with other functional proteins, such as enzymes or fluorescent proteins, using genetic engineering techniques. This method enables multifunctional nanobodies to be created with enhanced stability and activity, but may require extensive optimization and validation. We used this method to fuse E11 with mKappa VHH – a nanobody that targets the light chain kappa region of mouse IgGs.

Bioorthogonal click chemistry: This method involves the specific reaction between bio-orthogonal functional groups, such as azides and the dibenzocyclooctyne group (DBCO), which can be conjugated to nanobodies and other molecules. Click chemistry enables precise and selective functionalization of nanobodies to synthesize non-conventional C to C fusions. We used this method to conjugate the E11 with hKappa VHH – a nanobody that targets light chain kappa region of human IgGs.

Chemical conjugation: Nanobodies can be conjugated to various chemical groups, such as fluorescent dyes, biotin, or drugs, using chemical crosslinkers. In the later sections we describe conjugation of a range of compounds such as biotin, rhodamine etc. to E11, using sortagging reactions for numerous applications.

2.2.1 Synthesis of the E11 and E11-mKappa VHH Genetic Fusion (GF)

Producing conventional antibodies in bacteria is challenging due to their large size, multi-subunit structure, post-translational modifications (glycosylation, disulfidebridges etc) , and their tendency to aggregate. However, bacterial systems offer an efficient platform for high-yield production of nanobodies. Careful optimization of the expression vector, host strain, induction conditions, and purification strategy can lead to the successful production of large quantities of functional nanobodies for various applications[22,34,35]. Here, we report our synthesis strategy to achieve high yield production of the different nanobody players used in this project.

Briefly, coding sequences of E11 and E11-mKappa VHH genetic fusion containing a C-terminal sortase motif and 6x His tag were cloned into the pHEN6 (an *E. coli* periplasmic expression vector) via Gibson assembly. Successful cloning was confirmed by DNA sequencing . WK6 *E. coli* cells were transformed using the cloned construct for each of the proteins. A VHH Production Protocol (optimized by members of the Ploegh lab) was used to express and purify each of these proteins. Yields of **20.9 mg/L** and **12.9 mg/L** were obtained for E11 and E11-mKappa genetic fusion respectively (after fast protein liquid chromatography (FPLC) purification.

All protein products were purified using FPLC and analyzed on 15% SDS/PAGE gels to assess purity **(Figure 3A).**

2.2.2 Synthesis of E11-hKappa VHH Chemical Fusion (CF) using click-chemistry

Genetic fusions can be used to create C-to-N and N-to-C fused recombinant proteins, but they are not suitable for generating N-to-N and C-to-C fusion proteins. A click chemistry-based approach provides a simple way to create chimeric proteins of this kind. The technique involves equipping the N- or C-terminus of the target proteins with a set of click handles using Sortase A, followed by a strain-promoted click reaction. This procedure makes it possible to create unnatural C-to-C and N-to-N linked (hetero) fusion proteins[23].

Azide-DBCO (Dibenzocyclooctyne) click chemistry is a type of reaction that involves the chemical functionalization of a molecule containing an azide group with another molecule containing a DBCO group. The mechanism of the Cu-free azide-DBCO click reaction involves the reaction of an azide group with a strained cyclooctyne alkyne in the DBCO molecule. The reaction proceeds through a 1,3-dipolar cycloaddition mechanism, forming a triazole linkage. The reaction begins with the azide group acting as a 1,3-dipole, which undergoes nucleophilic attack on the strained cyclooctyne alkyne in the DBCO molecule. Upon this nucleophilic attack, a reactive intermediate is formed. This intermediate is stabilized through a strained alkyne cycloaddition and then undergoes elimination of the cyclooctyne. This leads to the formation of a triazole linkage between the azide and DBCO groups[36].

One of the main advantages of azide-DBCO click chemistry is its specificity. Azide-DBCO click chemistry only occurs between molecules containing an azide group and a DBCO group, which allows for precise and controlled functionalization of biomolecules. Azide-DBCO click chemistry has been widely used for functionalizing a variety of biomolecules such as proteins, peptides, and nucleic acids for various different applications[37]. Its ease of use, specificity, and mild reaction conditions make it a powerful tool for a variety of research areas. We used this reaction to conjugate azide-labeled E11 with DBCO labeled hKappa VHH to create the chemical fusion.

Briefly, we incubated hKappa-DBCO with 1.2X molar excess of E11-azide overnight at 4°C with shaking. The identity of the fusion product was confirmed using a 15% SDS PAGE gel **(Figure 3B).**

2.2.3 Chemical conjugation of probes and labels

Chemical conjugation of probes and labels can be achieved using a variety of chemical reactions, including a sortagging reaction, maleimide-thiol chemistry, click chemistry etc. The choice of conjugation chemistry is dependant on the specific application and the functional groups available on the molecule of interest and the nanobody.

We primarily used a sortagging reaction to conjugate a variety of probes to E11. The use of sortase has several advantages over more traditional labelling methods: it is site-specific, simple, and versatile. Sortagging allows the attachment of a wide range of biomolecules to the protein of interest, including fluorescent dyes, biotin, and peptides. The reaction is efficient with high yields of labelled protein, and it does not require harsh chemical treatments or modifications of the protein of interest. Sortagging is therefore a valuable tool for protein labelling and has significant potential for a broad range of research applications[38].

The sortagging reaction involves a multi-step process that utilizes the bacterial enzyme Sortase A to covalently link a labelled biomolecule to a protein of interest. The first step involves the genetic installation of a short amino acid sequence containing the LPXTG motif to the protein of interest near or at its C-terminus, creating a ‘sortagging’ recognition sequence. The second step involves the synthesis of the labelled biomolecule with (an) N- terminal glycine residue(s). The third step activates

Sortase A using calcium ions and reducing agents. In the final step, the labelled biomolecule is incubated with the activated Sortase A and the protein of interest that carries the sortagging tag. Sortase A catalyzes the formation of a covalent bond between the glycine residue at the N terminus of the label and the threonine residue of the LPXTG motif, resulting in the attachment of the labelled biomolecule to the protein of interest[39].

We used this reaction to conjugate biotin to E11. Briefly, we incubated E11 with GGG-biotin overnight at 4°C with agitation. We added 200 µL Ni-NTA (Qiagen) beads to remove the unreacted substrates and purified the reaction product using a PD10 desalting column. **Figure S1** briefly summarizes the sortagging procedure. The identity of the biotinylated product was confirmed using LC/MS (**Figure S1C**). We employed sortagging to react: 1) E11 with GGG-rhodamine 2) E11 with GGG-azide 3) E11 with GGG-NOTA 4) hKappa VHH with GGG-BDCO. The same procedure was used for all the four reactions to conjugate their respective GGG-probes substrates. The conjugate products obtained from these reactions were later used for binding studies using Size Exclusion Chromatography (SEC), synthesis of the chemical fusion and Positron Emission Tomography (PET) imaging studies as described in **Table S2.**

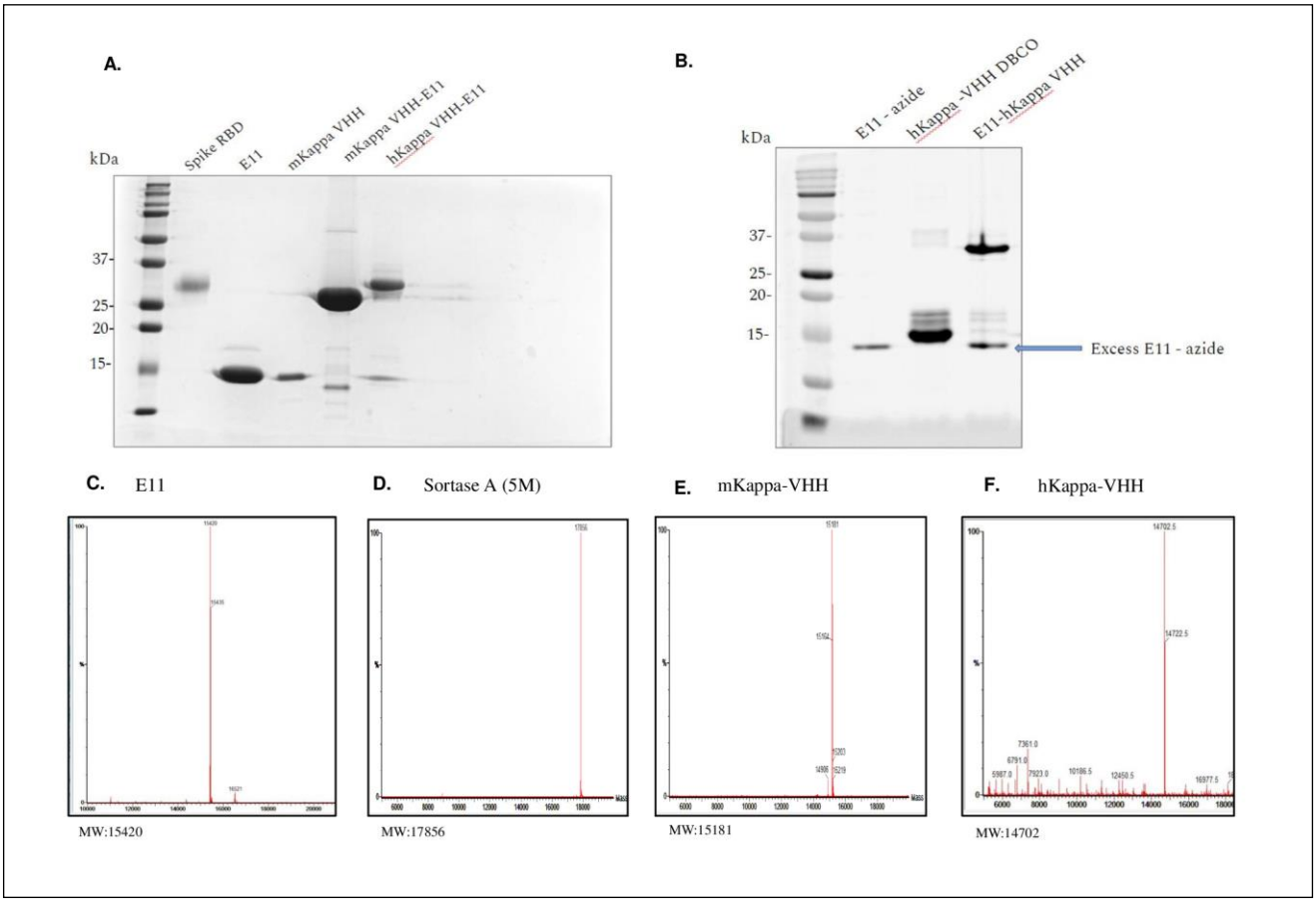

Figure 3: Synthesis of proteins used in this study. (A) Gel electrophoresis was used to confirm the synthesis of SARS-CoV-2 Spike RBD, E11, mKappa VHH, E11-mKappa VHH (GF), and E11-hKappa VHH (CF). (B) The Azide-DBCO click chemistry reaction was also verified through gel electrophoresis. The synthesized products of (C) E11, (D) Sortase A, (E) mKappa VHH, and (F) hKappa VHH were further confirmed using LCMS.

2.3 Binding studies

Validating the binding of the binders to their target is a critical step in the development of fusion proteins for their application, especially to avoid any off-target effects. We describe different approaches that were used to validate the binding capacity of the identified binders.

2.3.1 E11 shows signs of binding: SEC-based pilot studies

SEC (Size Exclusion Chromatography) is a widely applied chromatographic technique to study biomolecular interactions, such as protein-protein or protein-ligand interactions. SEC-based binding studies involve the use of SEC to separate and characterize the different species present in a mixture based on their shape and size. In a typical SEC-based binding study, a sample containing a mixture of molecules (e.g., a protein and a ligand) is loaded onto a SEC column[40]. As the sample passes through the column, smaller molecules penetrate deeply into the pores of the stationary phase and elute later. Whereas larger molecules are excluded from the pores. This allows them to pass through the column more quickly and thus they elute earlier. The elution profiles obtained from SEC can provide information about the molecular interactions between the components in the mixture. For example, changes in the elution profile of a protein in the presence of a another protein can indicate the formation of a protein-protein complex. In addition to providing qualitative information about molecular interactions, SEC-based binding studies can also be used to quantitatively determine the binding affinity between two molecules.

To check for binding between E11 and the RBD, we incubated about 200 µg spike RBD with a 4-5X molar excess of E11 nanobody. We subjected the mixture (volume 1 mL) to SEC on a Hi-Load16/600 S75 column (Cytivia). We then collected the peak fractions and analyzed them using a 15% SDS-PAGE gel and rhodamine fluorescence imaging. For the mixture of RBD and E11, we observed a shift in the peak that corresponds to the 'free' spike RBD in the FPLC elution profiles. A wavelength corresponding to rhodamine emission (568 nM) was detected under the RBD peak (shown in green), implying the formation of the RBD-E11 complex. Presence of the RBD and the E11-Rh conjugate in the fractions analyzed by SDS-PAGE further confirmed binding of E11 to RBD **(Figure S4)**.

A similar procedure was performed to check the binding of one of the peptide 6xkp_B_M_919 with the spike RBD. However, we observed neither a significant peak shift nor the presence of flurophore under the RBD peak in the elution profiles. We also did not detect any co-elution of the flurophore labeled peptide with RBD in the peak fractions that we analysed using SDS-PAGE and fluorescence imaging **(Figure S5)**.

FPLC may not be an optimal method to evaluate peptide binding to the RBD, especially for low-affinity binders, due to the significant size difference between the two molecules. To address this

concern, an alternative approach, Bio-Layer Interferometry (BLI), was investigated to determine its suitability for assessing peptide binding.

2.3.2 Computationally designed predicted peptides fail to bind: Peptide binding studies using BLI

BLI (Bio-Layer Interferometry) is a label-free biosensor technology that can be used to study the binding interactions between peptides and their target molecules. Compared to other techniques used to study binding interactions, BLI offers several advantages. Most importantly, it is capable of detecting even weak binding interactions. Furthermore, BLI allows real-time monitoring of the binding kinetics and affinity constants of small molecules, providing information about the nature and strength of the interaction.

We conducted BLI-based peptide binding studies in collaboration with Dr. Bradley Pentelute's lab at MIT. Four peptides predicted by the algorithm, namely 6xkp_B_M_919, 7kmg_C_A_47, 7l0n_R_A_312, and 7m7w_S_c_752, were tested along with two positive control peptides, SBP1 (an ACE2 derived peptide) and Biotin-1, which were previously reported by the Pentelute group[4142]. Briefly, we immobilized the biotinylated peptides onto the biosensor surface of streptavidin coated tips and then exposed it to a solution containing the SARS-CoV-2 RBD at different concentrations (250 nM-8 μM). The binding of the peptide to the target molecule causes a change in the interference pattern. Real time measurement of changes in the interference pattern is used to calculate the binding kinetics of the interaction.

Of the six peptides that we tested, only Biotin-1 showed signs of binding with apparent dissociation constant, K_D of 780 nM. SBP1 did not show any binding to the RBD. It was later discovered that SBP1 shows micromolar range binding only with insect-derived RBD. The rest four predicted peptides, 7kmg_C_A_47, 7l0n_R_A_312, and 7m7w_S_c_752 did not show any binding in the concentration range we tested and are likely to be low affinity binders, if they bind at all **(Figure S4)**. It is likely that these peptides do not maintain their bound conformation in solution. In the design phase we assumed that these peptides would retain the conformation of their bound state as their lowest energy conformation. This assumption did not take into account that the selected peptides are scaffolded by framework regions in the intact immunoglobulin. This suggests that such peptides require additional optimization such as circularization or a graft in D-pro-L-pro template to obtain stability in their structure. Previous studies have reported significant improvements in the binding abilities of the CDR derived linear peptides upon circularization[25]. Hence a future possibility would be to check if circulation could improve the shortlisted peptide binders.

Since none of the peptides were found to have binding affinity in the range of 1-100 nM, we proceeded with E11 as our only conserved spike protein binder for further studies.

2.3.3 E11 binds to SARS-CoV-2 spike protein and its variants: ELISA-based binding study

Since we obtained a promising lead with the E11 nanobody from the SEC studies, we tested the binding affinity of E11 to the recombinant spike RBD, SARS-COV-2 spike trimer (Wuhan, 2019) and the Omicron variants using ELISA.

ELISA (Enzyme-linked immunosorbent assay) is a highly sensitive and specific laboratory technique that can detect molecules at low concentrations, making it ideal for research, diagnostics, and quality control applications. It is versatile and can detect a wide range of molecules, including proteins, hormones, and antibodies. ELISA is cost-effective, requires simple equipment, and can be automated for high-throughput screening.

To investigate the binding affinity of E11, we immobilized RBD onto a 96-well ELISA plate at a protein concentration of 100 ng per well and blocked the plate with the blocking buffer (1X PBST+5%BSA). We then added purified E11 and conducted serial 3-fold dilutions. After an hour of incubation, we added streptavidin-HRP and tetramethylbenzidine (TMB), while including a wash step after evey addition. We also repeated the same procedure to test the binding of E11 with SARS-CoV-2 spike trimer and its Omicron variant (B.1.1.529).

Our results indicate that E11 has a nanomolar binding affinity for the SARS-CoV-2 Spike RBD (K_D = 1.17 nM), Wuhan-2019 SARS-CoV-2 spike trimer (K_D = 0.511 nM), and Omicron B.1.1.529 (K_D = 0.523 nM). These findings support our hypothesis that E11 targets a conserved site on the RBD and suggest that its binding affinity is unaffected by the mutations present in the latest SARS-CoV-2 variants.

.

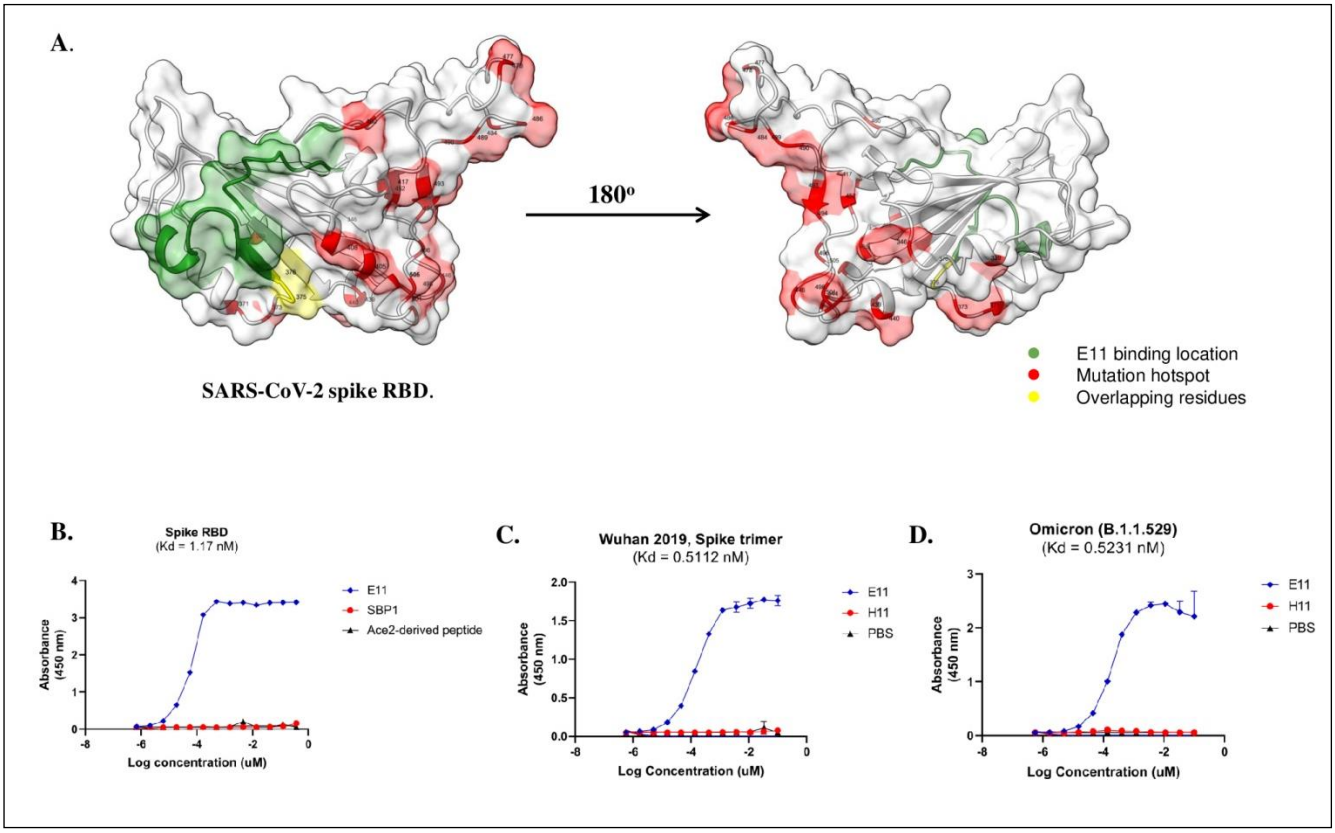

Figure 4. Structural and binding analysis of E11. (A) E11 binding location (in green) and mutation hotspot (in red) mapped on the RBD surface, along with the overlapping residues (in yellow). The small patch of overlap between the binding location and the mutation hotspot suggests that E11 targets a conserved site on the RBD. ELISA curves of E11 bound to (B) recombinant RBD, (C) Wuhan 2019 spike trimer, and (D) Omicron spike variant (B.1.1.529), respectively. Notably, no significant alteration in K_D value is observed, indicating the robust binding of E11 to these spike proteins.

2.3.4 E11- mKappa (GF) and E11-hKappa (CF) both bind to SARS-CoV-2 spike expressing cells and recruit polyclonal IgGs: Saturation binding assay

After validating the successful binding of E11, we next examined whether the E11 fusions can target the SARS-CoV-2 spike in vitro and recruit polyclonal immunoglobulins. To do so we performed saturation binding assays (SBA) with E11-mKappa VHH (GF) and E11-hKappa VHH (CF).

Saturation binding assays (SBA) can be performed in a cell-based format, which involves the use of intact cells rather than isolated receptors. In this case, cells are incubated with varying concentrations of radiolabeled ligand. The measurement of amount of bound ligand provides an estimate on the strength of binding. Cell-based saturation binding assays offer several advantages over isolated receptor assays, as cells provide a more physiological environment and can take into account the effects of the cell membrane and cytoplasmic components on ligand binding. Moreover, cell-based assays can provide information on the distribution and localization of receptors within the cell, which can be useful for exploring the receptor expression level and density at the cell surface[43].

We used HEK293 cells that express the SARS-CoV-2 spike protein on its surface, to perform saturation binding assays with the E11-hKappa VHH (CF) and E11-mKappa VHH (GF). We grew

HEK293 cells expressing SARS-CoV-2 spike protein in humidified incubators at 37°C, 5% CO_2. We used HEK293 cells that do not express the spike protein as the negative control. We loaded 10,000 cells per well onto an lysine coated 24-well plate and performed serial 4X dilutions with a starting concentration of 200 nM for both E11-hKappa VHH (CF) and E11-mKappa VHH (GF), followed by incubation with fluorescently labelled anti-human Ig and anti-mouse Ig respectively. After three rounds of washing with DMEM, cells were lysed using Sodium Dodecyl Sulfate (SDS) detergent. We used the fluorescence of Human IgG-Phycoerythrin (PE) and Mouse IgG-Phycoerythrin (PE) to quantify the amount of E11-hKappa VHH (CF) and E11-mKappa VHH (GF) bound to spike protein on the cell surface.

We observed a nanomolar binding affinity for both the fusions, E11-hKappa VHH (K_D = 2.08 nM) as well as E11-mKappa VHH (K_D = 0.503 nM).

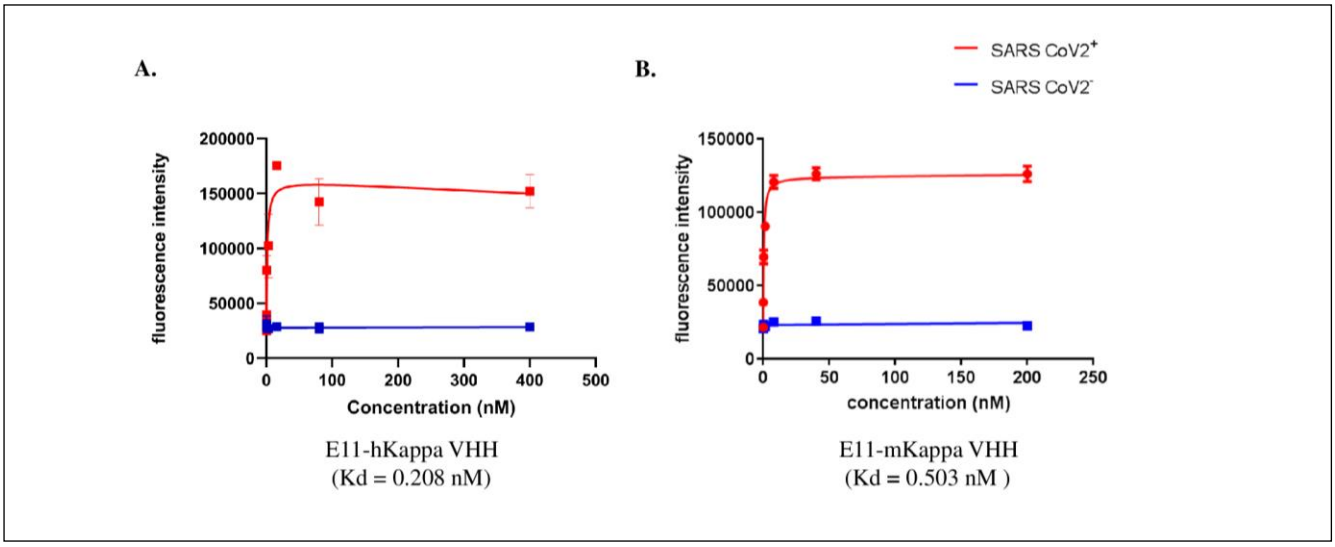

Figure 5. Binding of nanobody fusions and IgG recruitment. Saturation binding curves of (A) E11-hKappa VHH (CF) and (B) E11-mKappa VHH (GF) to the SARS-CoV-2 spike expressing and non-expressing HEK293 cells.

2.4 Activation of effector functions

We next tested if the nanobody fusion could activate the effector functions of the non-specific antibodies that it recruits. We tested activation of two mechanisms namely, Complement-dependent cytotoxicity (CDC) and Antibody-Dependent Cellular Cytotoxicity (ADCC).

2.4.1 E11-mKappa (GF) and E11-hKappa (CF) both activate CDC at nanomolar concentrations: CDC assay

Complement-dependent cytotoxicity (CDC) is a process by which molecules of the immune system destroy harmful pathogens or infected cells through the activation of the complement system[44]. The complement system is a group of proteins that work together to eliminate foreign substances from the body[45].There are three distinct ways in which the complement system can be activated namely, the

classical pathway, the lectin pathway and the alternative pathway[46]. Each pathway involves a series of enzymatic reactions that ultimately result in the formation of a membrane attack complex (MAC). Pore formation in the membrane of the target cell is initiated by the MAC complex, leading to its lysis[47].

This type of complement-mediated cell lysis occurs when antibodies bind to the an antigen expressing on target cell surface. Normally, when antibodies bind to the target cell surface, they activate the classical pathway of the complement system, thereby initiating the formation of the MAC complex. In our case, the nanobody fusions would activate this effector function of non-specific antibodies and lead to the formation of a MAC. The formation of the MAC on the target cell surface will result in the influx of ions and water into the cell, causing it to swell and eventually burst. This process is effective at eliminating pathogens or infected cells, as it allows the immune system to rapidly destroy large numbers of cells[48].

To examine if the E11-mKappa VHH genetic fusion could activate CDC, we loaded HEK293 cells expressing SARS-CoV-2 spike protein into a 96-well plate at a concentration of 10,000 cells per well. The plate was then divided into two groups. The first group and the second group were incubated with E11-mKappa VHH fusion and the mixture of E11 and mKappa VHH, respectively, at a concentration of 10 nM for 30 minutes. We then add polyclonal mouse IgG and rabbit complement preserved serum and incubate for 6.5 hours at 37 °C. The viabilities of cells were measured using CellTiter-Glo® 2.0 Viability Assay (Promega). To quantify %CDC, the following formula was used:

$$\%CDC = \frac{\text{luminescence (no VHH) - luminescence (expt) X 100}}{\text{luminescence (no VHH) - luminescence (max killing)}}$$

The statistical difference of % cytotoxicity between the two groups was analyzed using a Student's t-test. A similar procedure was repeated substituting E11-mKappa (GF) with E11-hKappa (CF) at 100 nM concentration and mouse IgG with human IgG to check the efficacy of the chemical fusion.

The nanobody fusions resulted in a significantly higher level of cell death through CDC, compared to a mixture of their individual components (**Figure 6**). This suggests that both E11-mKappa VHH (GF) and E11-hKappa VHH (CF) can induce CDC in vitro over a range of concentrations **(Figure S5)**. The low level of cell death observed in the control groups indicates that the fusions do not have any non-specific cytotoxic effects.

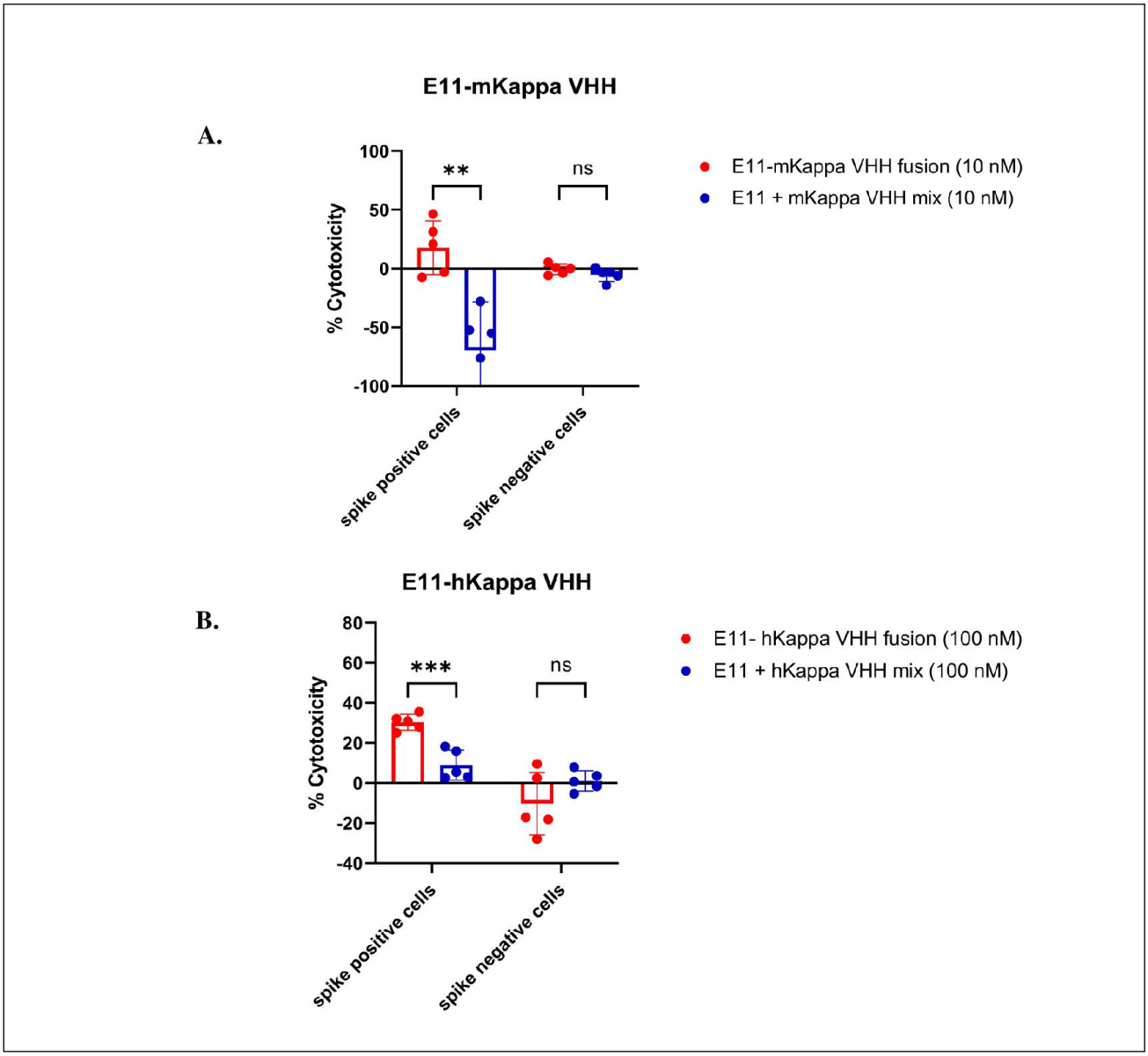

Figure 6. CDC activation. Percentage cytotoxicity of (A) E11-mKappa VHH (GF) and a mixture of E11 and mKappa at 10 nM concentration, (p=0.003321) (B) E11-hKappa VHH (CF) and a mixture of E11 and hKappa at 100 nM concentration (p=0.000492), quantified using CellTiter-Glo® Luminescent Cell Viability Assay for HEK293 cells expressing SARS-CoV-2 spike protein and WT-HEK293 cells.

2.4.2 ADCC: A possibility

ADCC (Antibody-Dependent Cellular Cytotoxicity) is a crucial mechanism of the immune response against viruses and cancer cells. The activation of immune cells against a target cell, such as a virus-infected or cancer cell, can be initiated by the interaction of specific antibodies with antigens on the cell's surface. This binding event causes a change in the shape of the Fc region of the antibody, which enables it to bind to the Fc receptor found on immune cells, like the natural killer (NK) cells, macrophages, and neutrophils.

When the Fc region of an antibody binds to the Fc receptor on the surface of an immune cell, it initiates a signaling cascade within the cell. This cascade can trigger the release of cytotoxic

molecules, including perforin and granzymes. These molecules can create pores in the membrane of the targeted cell, leading to apoptosis or programmed cell death of the targeted cell[49].

Besides the Fc receptor, other molecules on the immune cell surfaces, such as CD16 and CD64, also play important roles in triggering ADCC. These molecules can bind to the Fc region of antibodies and initiate the signaling pathways that lead to the destruction of the target cell[50].

Various factors can impact the efficiency of ADCC, such as the affinity of the antibody towards its target antigen, the antigen density on the target cell surface, and the activation state and quantity of immune cells present in the microenvironment[51].

Overall, the triggering of ADCC is a complex process that is not fully understood and involves multiple interactions between antibodies, antigens, and immune cells[52]. Here we tried to explore if our fusions could activate the ADCC process.

To determine if the fusion molecules could initiate ADCC and selectively eliminate infected cells, we conducted ADCC assays using various treatment methods to identify the optimal conditions. HEK293 cells expressing the SARS-CoV-2 spike protein, were added to a 96-well plate at a density of 10,000 cells per well. The plate was then divided into two groups, each subjected to a distinct set of treatment conditions.The first group was incubated with E11-mKappa VHH fusion and the second group was incubated with a mixture of E11 and mKappa VHH at four different concentrations (0.1 nM, 1 nM, 10 nM, and 100 nM) for 30 minutes. A similar procedure was followed with WT-HEK293 cells as a negative control. Cells were then subjected to different conditions described in **Table S3** with ADCC Bioassay reporter cells (Promega), unfractionated splenocytes, and BMD-NK cells in three different cases. Viability of the cells was measured using the CellTiter-Glo® 2.0 Viability Assay. The effector cell's luminescence was quantified to determine cell based on the viability luciferase activity, in case ADCC Bioassay effector cells treatment group.

We observed no notable difference between the fusion and mixture groups in the case of unfractionated splenocytes and ADCC Bioassay effector cells (**Figure S6 and Figure S7**). However, we did observe a slight difference in the case of the (Bone Marrow derived) BMD-NK cells (**Figure S8)**. This difference, however, was not statistically significant. Further optimization of the assay may be required.

There could be several reasons why we did not observe activation of ADCC. One possibility is that the expression of spike protein on the transduced HEK293 cells may not have been sufficient. Another possibility is that the fusions failed to induce the conformational change in the recruited antibodies needed to trigger ADCC. The low frequency of NK cells (that are primarily responsible for ADCC) in unfractionated splenocytes (only 2-4%), may not have been sufficient to produce the necessary effector-to-target cell ratio for ADCC activation. Another potential reason could be that the transduced HEK293 cells were resistant to cell lysis by the effector cells, in which case testing with a real SARS-CoV-2 virus or VSV pseudo-virus and a suitable ACE2 receptor-expressing cell line

would be necessary. Since ADCC effectiveness is influenced by several factors, the substitutes used in the in vitro assays may not be an accurate representation of a real virus-infected cell.

Other studies conducted at the Ploegh lab have reported that this fusion strategy can initiate ADCC in case of real virus infections, also in vivo. For example, the zanamivir-mKappa VHH fusion molecule, which targets the neuraminidase, has shown to activate ADCC successfully in MDCK cells when infected with real influenza virus (**Figure S9**). Based on these observations, we speculate that ADCC may be possible in the case of the SARS-CoV-2 virus, if tested with real SARS-CoV-2. However, this is beyond the scope of this project due to the safety measures required.

2.5 Crystallisation and *in vivo* localisation of E11

The precise determination of the binding site of E11 and RBD is valuable in gaining insights into E11's effectiveness in targeting the latest variants of concern. In this section, we aimed to determine the crystal structure of the E11-RBD complex to gain a deeper understanding of the binding interaction between these two molecules. We are also currently investigating the in vivo localization of E11 to spike-expressing cells to further enhance our understanding of its target binding abilities.

2.5.1 Solving the structure of E11-RBD complex: Crystallisation

The determination of the 3D structure of protein complexes relies on the essential step of crystallization[53]. It involves the formation of an ordered array of protein molecules in a highly purified solution, which then undergoes a process of crystal lattice formation. The process of crystallizing protein complexes is intricate and influenced by several factors such as the concentration of protein, pH, temperature, chemicals like salts or ligands. Often, a trial-and-error approach is used to determine the optimal conditions for crystal formation[54].

Once protein crystals are obtained, they are subjected to X-ray diffraction to determine the protein complex's atomic structure. This technique involves irradiating the crystal with an intense beam of X-rays, which diffracts the beam into a pattern of spots. The pattern is then analyzed to determine the electron density distribution of the protein complex[55].

To solve the crystal structure of E11-RBD complex we first incubated 2.02 mg of RBD with 2X molar excess of E11, purified it using SEC and concentrated the mixture to 13 mg/ml. In collaboration with Dr Thomas Schwartz's Lab, droplets were set up in hanging drop conditions using an Art Robbins Phoenix micropipetting robot (a Formulatrix Formulator robot) at MIT. Crystals were obtained at room temperature in six different conditions described in **Figure S10**. However, none of the crystals showed diffraction beyond a resolution of 10 Å, which suggests the need for further refinement to obtain better crystals. An optimization of conditions is currently underway to obtain better resolving crystals.

2.5.2 Localization of E11 to its target *in vivo*: insights from PET imaging studies

PET is a non-invasive imaging method used to examine the *in vivo* behavior of biological molecules including medicines, antibodies, and proteins[56]. PET imaging studies provide insights into the localization of these molecules within the body and their interaction with target molecules. By labeling the molecules of interest with radioactive isotopes, one can track the distribution and metabolism of drugs *in vivo* and gain insights into the mechanisms of drug action and resistance[57].

To study localization of E11 *in-vivo*, we introduced xenografts of spike expressing HEK293 cells and WT HEK293 in two separate groups of female athymic NU/J mice. At 22 days post- implantation, PET imaging of dual tumours was performed using radiolabeled ^{64}Cu-E11-NOTA and ^{64}Cu-E11-NOTA-$PEG_{20.}$ To mitigate the impact of partial volume effects of the tumor, we conducted a region-of-interest (ROI) analysis on the obtained images.

A strong labelling was observed in the tumour region for spike-expressing HEK293 for both ^{64}Cu-E11-NOTA and ^{64}Cu-E11-NOTA-PEG_{20} **(Figure S10A**). The signal was observed to increase with time in case of ^{64}Cu-E11-NOTA suggesting accumulation of the compound in the tumours **(Figure S11C)**. Whereas in case of ^{64}Cu-E11-NOTA-PEG_{20}, the signal remained fairly constant throughout all the time points (**Figure S11D**).

The WT-HEK293 tumours also showed a strong signal, suggesting non-specific labelling of the tumour (**Figure S10B**). This observation can be attributed to the fact that the tumour size of WT-HEK293 were found to be substantially bigger as compared to the Spike-expressing HEK293 tumours **(Figure S11).** Bigger tumours tend to show larger amounts of vascularisation indicating higher circulation of the compounds in the tumour region. Another factor that must be taken into consideration is the surface level expression of spike protein in the transduced HEK293 cells. Tumour models may not an accurate representation for this study. Hence, imaging experiments of E11 localisation in real virus infected Cynomogus monkeys are currently underway - in collaboration with the Primate Research Centre in Netherlands.

Chapter 3 Materials and Methods

3.1 Structure-based design of the peptide binders

A 212 spike-bound antibody structure database was obtained from RCSB PDB Covid19 Resources (as of June 2021). Antibody sequences in the PDB database are generally numbered using schemes like those developed by Kabat or Chothia. We found that this non-conventional numbering scheme interferes with the recognition process of residue locations at multiple steps in our peptide design process. So all the PDB structures were renumbered, and the missing residues were added using the complete_PBD command in MODELLER v10[58].

Cell list, a tool for efficiently finding all the neighbours of any atoms within some cut-off distance, was used to identify interchain distances for each of the 212 structures. If any pair of atoms from neighbouring chains fell within a cut-off of 5 Å, the chain pair was selected as an interacting chain pair. The features of the atomic interaction from these chains were recorded in the Cell list output files. Keywords such as *SARS-CoV-2 Spike glycoprotein*, *Spike protein S1* etc. were then used to identify the chains corresponding to the spike protein in the structure complexes. Using the information, inter-spike chain pairs were eliminated, and only the spike-antibody interacting chains were retained. We obtained 920 spike-antibody interchain interacting pairs in total. The cell list output files were then processed to identify contiguous stretches of amino acids with more than 6 interacting (- interchain residues that lie within the radius cutoff of 5 Å) residues and a maximum allowed gap of 3 non-interacting residues. Such peptide stretches were selected from the antibody chain and were referred to as the spike-binding peptide candidates. Redundant peptides were eliminated based on the peptide sequence similarity. We obtained 275 unique peptide sequences using the above-mentioned selection criteria.

3.2 Computational binding validation of peptide-protein complexes

Modelling: Using MODELLER v10.1 and crystallographic structures from the database, models of peptides bound to the SARS-CoV-2 spike RBD were built for all the peptides derived in the library. As a positive control, we built a model of an N-terminal helix peptide derived from the ACE2 receptor using the ACE2-spike complex structure (PDB id: 6M0J) following the exact same criteria of peptide selection described above.

FoldX scoring: FoldX, an empirical force field that can quickly examine the dynamics and stability of protein complexes, was used to score the models in order to compare the binding energies of the peptides in the library with the control peptide. We employed the 'AnalyseComplex' command to calculate the binding energy of the protein-peptide complex. It works by unfolding the selected complexes, determining if the remaining molecules are stable, and then subtracting the total of the individual energies from the global energy. The Gibbs energies of the complex (ΔG_{AB}) and the two molecules A and B alone are computed by FoldX in order to determine the free energy of binding of a complex AB.The binding energy is then calculated as: $\Delta G_{binding} = \Delta G_{AB} - (\Delta G_A + \Delta G_B)$[28,59]. We set the FOLDX binding energy of the control peptide as a cutoff score to shortlist peptides that could potentially compete with the wild-type receptor**.**

PIZSA: We also used PIZSA, a statistical tool that assesses protein-protein interactions based on atomic propensities and preferences for interface residue pairing[29].

MD simulations: Protein-peptide complexes that met the binding energy cut-off set by the control peptide underwent further investigation using molecular dynamics simulations. The simulations were run on the CHARMM27 force field and GROMACS software package with the systems solvated in a water box and counter ions added for charge neutrality[60,61]. The simulations were run for three rounds to ensure the stability and binding of the peptides, with the protein-peptide inhibitor complexes simulated for a maximum of 50 ns. Triplicate runs were found to be consistent for all the shortlisted set of peptides **(Figure S13**).

3.3 Cells

Culturing of Expi293F and HEK293 cells: Expi293F cells were cultured in humidified, shaking incubators at 37 °C, 8% CO_2 in Expi293 Expression Media. Wild type HEK293 cells and Wuhan-Hu-1 SARS-CoV-2 Spike protein-expressing HEK293 cells (InvivoGen) were maintained under the same conditions in Dulbecco's Modified Eagle Medium (DMEM) with 10% FBS and 1% Penicillin-Streptomycin.

Extraction of bone marrow derived Natural Killer (NK) cells and splenocytes: Bone marrow was extracted from the tibiae and femur regions of C57BL/6J (B6) mice. Bone marrow cells were then flushed using injection and cultured in Dulbecco's Modified Eagle Medium (DMEM) with 10% FBS and 0.02% beta-mercaptoethanol. RBCs in the mixture were lysed by incubating the mixture in ammonium chloride solution (0.8% NH_4Cl and 0.1 mM EDTA in MilliQ water at pH of 7.4) for 10 minutes. Growth of NK cells was selectively promoted by addition of 0.1 % IL15 in the culture. Unfractionated splenocytes were obtained by expelling cells from a spleen obtained from a C57BL/6J

(B6) mouse, followed by RBC lysis as described above. About 80 million viable splenocytes were recovered, which were then used for the ADCC Assay.

3.4 Peptides, proteins and probes

Peptide synthesis and modifications: The lyophilized powder peptides were acquired from GenScript and then reconstituted in dimethyl sulfoxide (DMSO) at a concentration of 1 mg/mL. These were further purified using HPLC.

A cysteine moiety was introduced at the N terminus of all peptides to allow conjugation of the peptide with a fluorophore (Table. S1). Fluorescein-5 Maleimide was used for the peptide- fluorophore labeling at the N terminus. Biotin-$(PEG)_3$-Maleimide was used for Biotinylation of the peptides at the N terminus. Lyophilized peptides were resuspended in DMSO (Dimethyl sulpoxide) and incubated with flurophore/biotin maleiamide at room temperature overnight with stirring for reaction. The conjugate products of the reaction were further purified using HPLC and confirmed using LC-MS **(Figure S14).**

Cloning and Expression of E11 and E11-mKappa VHH: Coding sequences for E11 and E11-mKappa VHH fusion with a C-terminal sortase motif and 6x His tag were cloned into the pHEN6 (a periplasmic expression vector). WEK6 *E. coli* were transformed with the cloned vectors and grown to mid-log phase at 37 °C in terrific broth with ampicillin.The cultures were then induced with 1 mM IPTG overnight at 30 °C. Proteins were harvested by centrifugation at 6,000 × g for 20 minutes at 4 °C. The cells were resuspended in 15 mL of 1× TES buffer per liter culture and incubated at 4 °C with shaking for 1 hour. Osmotic shock was induced by performing a 4x dilution of the TES buffer with ice cold MiiliQ water and overnight incubation at 4 °C. The periplasmic fraction was isolated by centrifugation at 8000×g for 20 minutes at 4 °C and then loaded onto chromatography columns containing Ni-NTA resins. Following 3 washes with PBS, the Ni-NTA bead captured proteins were incubated with 10 mM imidazole. The proteins were next eluted in phosphate-buffered saline (PBS) and further purified using FPLC. Peak fractions were pooled and SDS/PAGE was used to assess the purity of the recombinant VHHs.

Protein Expression and purification of Spike RBD: The pcDNA3.1(-) vector, which carries the RBD of the Wuhan-Hu-1 Spike Glycoprotein, was acquired from BEI Resources. Polyethyleneimine (PEI) was used to transfect Expi293F cells with the construct, which were then cultured in Expi293 Media at 37°C for 4 days. The proteins were collected through centrifugation at 6,000×g for 20 minutes at 4°C, followed by purification using Ni-NTA beads and size exclusion chromatography using a Hi-Load16/600 S75 column (Cytivia). The proteins were analyzed using 15% SDS/PAGE, and the gels were stained with Coomassie blue **(Figure 2)**.

Sortase A (5M) Production and Purification: A glycerol stock of WEK6 *E. coli* transformed with pET-30 b (+) vector for sortase A (5M) expression was available in the Ploegh lab. The bacterial culture was grown in Terrific Broth containing ampicillin at 37 °C until mid log phase. Induction was performed by adding 1 mM IPTG and incubating overnight at 30 °C. The cells were harvested by centrifugation at 6,000 × g for 15 min at 4 °C, resuspended in 1× TES buffer (consisting of 200 mM Tris, , 0.5 M sucrose and 0.65 mM EDTA) at a ratio of 15 mL per liter of culture. The mixture was then incubated at 4 °C with shaking for an 1 hour. The cells were then lysed by passing through a homogenizer three times at 14,000 p.s.i. The cytoplasmic fraction was obtained by centrifugation at 12,000 × g for 30 min at 4 °C. This was then loaded onto Ni-NTA (Qiagen) beads in PBS and eluted with PBS. The protein was purified using FPLC. Sortase A (5M) was analyzed by 15% SDS/PAGE, and the peak fractions were pooled, concentrated and stored at −80 °C.

Sortase A (5M) mediated conjugation of probes and click handles: A sortase reaction was used to conjugate GGG-rhodamine with the E11 nanobody containing the sortase recognition motif **(Figure S1A**). 1 mL reaction is set up by incubating 100 µM E11 with 5X molar excess GGG-rhodamine overnight at 4°C with agitation in presence of sortase A and $CaCl_2$. After the reaction, 200 µL Ni-NTA (Qiagen) beads were mixed with the mixture to separate the unreacted substrates. The reacted product was purified using a PD10 column. The reaction product was confirmed using a rhodamine blot (**Figure S1**). A similar procedure was followed to conjugate Biotin, azide, DBCO and NOTA on different substrates.

3.5 Binding experiments

Size Exclusion Chromatography: 200 µg of RBD was incubated with 4-5X molar excess of E11 nanobody for 1 hour. The mixture (volume 1 ml) was then subjected to a size exclusion chromatography using a Hi-Load16/600 S75 column (Cytivia). Peak fractions were collected and analyzed with 15% SDS PAGE gel and rhodamine blot. Similar process was followed for the control peptide-RBD binding study.

Bio-layer interferometry: The BLI studies were performed in collaboration with Pentelute lab at MIT. Biotinylated peptides (1−4) were synthesized in-house using maleimide chemistry described previously. Identity of the biotinylation products was confirmed using LC/MS. Two additional tight binding peptides reported by the Pentelute group – SBP1 and Biotin 1 were used as positive controls for the BLI studies. Streptavidin-coated biolayer interferometry (BLI) tips were used to immobilize the biotinylated peptides and measure the association and dissociation of SARS-CoV-2-spike-RBD at varying concentrations, starting with 8 µM followed by 2x dilutions. was used To validate the in vitro

peptide-protein binding Gator® Pro Bio-Layer Interferometry system was used at 30 °C and 1000 rpm. For the loading step, the streptavidin tips were dipped in 200 µL of biotinylated peptide dissolved in 1x kinetic buffer solution (1xPBS with 0.1% BSA and 0.05% tween) at a concentration of 200 nM. The loaded tips were first dipped in wash buffer to remove any nonspecific binders. These tips are next dipped in SARS-CoV-2-RBD at various concentrations in 1xkinetic buffer to obtain the association curve. Following association, the tips were re-dipped in 1xkinetic buffer to get the dissociation curve. The dissociation constant K_D was calculated using Gator® Screener Software by fitting the association and dissociation curves.

ELISA: To prepare the microplates for experimentation, high binding 96-well ELISA plates (obtained from Costar, NY, USA) were coated with 1 µg/mL of SARS-COV-2 RBD in PBS at 4 °C overnight. Subsequently, the plates were blocked using the blocking buffer (consisting of PBST with 5% BSA) for 2 hours at room temperature. In the first group of wells, biotinylated E11 was added at a concentration of 100 nM. Binding of different concentrations of biotinylated E11 was checked by performing a three-fold serial dilution. After an incubation period of 2 hours, the plates were washed using wash buffer (consisting of PBS with 0.05% Tween-20) and incubated at room temperature for an hour, with Streptavidin-HRP (horseradish peroxidase) which was diluted 1:5000 in the blocking buffer. Following three washes with PBST, tetramethylbenzidine (TMB) substrate was added to the plates and the reaction was allowed to develop for 15 min. The reaction was ceased by the addition of equal volume of 1 N HCl. The absorbance was measured at 450 nm. A similar protocol was performed, with Spike RBD being substituted with other following targets of interest, to determine the binding of E11 with the SARS-CoV-2 Wuhan-Hu-19 spike trimer and the Omicron variant (B.1.1.259), which were obtained from a commercial vendor (Sino Biologicals).

Saturation binding assay: HEK293 cells expressing SARS-CoV-2 spike protein were grown in humidified incubators at 37 °C, 8% CO2 with Dulbecco's Modified Eagle Medium (DMEM). Normal HEK293 cells that do not express the spike protein were also grown using the same conditions as the control group. 10,000 cells per well were loaded onto a high affinity 96-well plate. A 4X serial dilution was performed with a starting concentration of 200nM for both E11 and E11-mKappa VHH fusion. The fluorescence of conjugated rhodamine and Mouse IgG-Phycoerythrin (PE) were used to quantify the amount of E11 and E11-mKappa VHH fusion bound to spike protein on the cell surface respectively.

3.6 CDC and ADCC experiments

CDC Assays: A 96-well plate was prepared with HEK293 cells that expressed the SARS-CoV-2 spike protein, with a concentration of 10,000 cells per well. The plate was next incubated at 37 °C, 8% CO2 overnight. The plate was then divided into two treatment groups. The first and the second groups were incubated with E11-mKappa VHH fusion and the mixture of E11 and mKappa VHH respectively at the same concentration of 10 nm for 1-1.5 hours. Both the groups were incubated with polyclonal mouse IgG (200 nM) and rabbit complement preserved serum (20% v/v) for 6.5 hours at 37°C. In case of testing the cytotoxicity by E11-hKappa VHH chemical fusion, the treatments was substituted with E11-hKappa VHH fusion and the mixture of E11 and hKappa VHH followed by addition of polyclonal human IgG (200 nM) and rabbit complement preserved serum (20% v/v) with same incubation time. Cell viability was measured using CellTiter-Glo® 2.0 Viability Assay (Promega). CDC was quantified using the following formula:

$$\%CDC = \frac{\text{luminescence (no VHH) - luminescence (expt)}}{\text{luminescence (no VHH) - luminescence (max killing)}} \times 100$$

Statistical difference of %cytotoxicity between two groups was analyzed using t-test.

As a negative control, WT HEK293 cells were used instead of spike-expressing HEK293 cells and the same procedure was followed to evaluate the cytotoxicity.

ADCC Assays: The assays were performed under three different conditions to search for optimum conditions of ADCC. For all the experiments, HEK293 and spike expressing 293 cells were loaded onto two different white opaque bottom 96-well plates at a concentration of about 10,000 cells/well. Following an incubation period of 37 °C with 5% CO2 that lasted overnight, the plates were exposed to four different conditions as outlined in **Table S3**. The choice of treatment applied was dependent on the particular assay protocol being employed. Each of the treatment methods was tested at four distinct concentrations. Mixtures of the individual components of the fusion were used at the same concentration as negative controls. Polyclonal mouse/human IgGs were added at a concentration of 200 nM to each well. With the exception of the ADCC reporter Bioassay, the CellTiter-Glo® 2.0 Viability Assay was used to detect cell viability. Luminescence intensity (RLU) was measured as a readout corresponding to the amount of viable cells per well. Statistical difference of RLU between two groups was analysed using t-test.

3.7 Crystallization of SARS-CoV-2 RBD–E11 complex

In order to obtain a purified SARS-CoV-2 RBD-E11 complex, 2.02 mg of SARS-CoV-2 RBD was mixed with a 2X molar excess of E11 in a 20 mM Tris and 150 mM NaCl solution and incubated on

ice for an hour. The mixture was then subjected to size exclusion chromatography, and the complex containing fractions were identified through 15% SDS PAGE. These fractions were combined, and the resulting mixture was concentrated to a final concentration of 13 mg ml−1

To create the drops, the SARS-CoV-2 RBD-E11 complex in 20 mM Tris pH 7.5, 150 mM NaCl was mixed with 200 nl of well solution using an Art Robbins Phoenix micropipetting robot at MIT. The drops were set up in hanging drop conditions with a Formulatrix Formulator robot to generate custom screens. Several screening conditions were established to identify crystals with better resolution. The crystals of E11-RBD complex were successfully grown at room temperature in six different conditions shown in **Figure S10.**

The data collection process was conducted at the Advanced Photon Source end station situated at Argonne National Lab. Most crystals failed to diffract. For a few, the diffraction data was obtained at a wavelength of 10 Å. Given the low resolution of the crystal complex, a finer refinement of conditions is required to solve the crystal structure.

3.8 PET imaging studies

Synthesis of Radiolabeled ^{64}Cu-E11-NOTA and ^{64}Cu-E11-NOTA-PEG-20: The E11-NOTA and E11-NOTA-PEG_{20} were radiolabeled with ^{64}Cu as follows: On Day 1, 1 to 1.5 mg of purified E11 was mixed with GGG-NOTA-Azide in presence of Sortase A (5M). The mixture was incubated overnight on a shaker at 4°C. The compound was purified on day 2, using Ni-NTA beads. PEG_{20}-DBCO was then added to half of the purified sample in 5X molar excess and incubated overnight at 4°C with shaking. The remaining half was used for ^{64}Cu-E11-NOTA synthesis. Around 3 mCi ^{64}Cu was added to 500 µl of E11-NOTA and E11-NOTA-PEG_{20} each. The solutions were incubated for about an hour at room temperature with shaking, and then purified using PD10 columns individually. Radioactivity levels were checked for each fraction to determine which fraction to use for imaging. The fraction with highest recovery of radioactivity was used for retro-orbital injections into mice

Tumour Grafting: Spike-expressing HEK293 and HEK293-WT cells were implanted in the thigh region of female athymic NU/J mice (8 weeks old, Jackson Laboratory) at a concentration of 5×10^6 cells suspended in 200 µL of cell culture medium/matrigel (1:1/ v:v). Imaging was performed at 22 days post-implantation, once the tumor had grown significantly.

PET/CT Imaging: Two groups of mice were given retro-orbital injections of either 100 µCi of 64Cu-E11-NOTA (n=2) or 64Cu-E11-NOTA-PEG20 (n=3). PET/CT imaging was performed on the G8 Multimodal PET/CT Imaging System (PerkinElmer) under 2% isoflurane anesthesia at 1, 5, and 20 hours after injection. PET scans were reconstructed using the VivoQuantTM Image Post-processing system, and the reconstructed data was rendered in three dimensions. To minimize partial volume

effects of the tumor, region-of-interest (ROI) analysis was performed on the images after 10 minutes of data acquisition on the PET scanner, followed by 2 minutes on the CT scanner.

Chapter 4 Conclusion

Many therapeutic monoclonal antibodies (mAbs) and vaccines have significantly lost effectiveness as a result of the emergence of multiple unique SARS-CoV-2 variants, notably the Omicron and its subvariants. As an unusually high number of mutations keep accumulating in the spike protein of these variants, identifying the conserved epitope on the spike trimer is an urgent need for the development of effective treatment methods.

In this study, we reported a conserved binder, E11, which targets most variants of SARS-CoV-2, including the B.1.1.529 (Omicron) strain. Our structural analysis predicts that E11 should be able to target all the latest variants with nanomolar binding affinity. However, the parallel approach of using CDRH3-derived peptides predicted by the computational algorithm was not successful in finding high-affinity spike binders and will require further optimization.

We demonstrated the high-yield production of E11-mKappa fusion in the bacterial expression system, which suggests a significant advantage over the limitations posed in synthesizing monoclonal antibodies. We also reported the successful synthesis of a non-conventional C-C fusion using click chemistry. This may be useful in certain situations, such as when specific chemical or structural properties need to be engineered.

Using SEC and ELISAs, we established the broad target binding capacity of E11. By using saturation binding assays, we also demonstrated the ability of fusions to recruit polyclonal immunoglobulin regardless of their specificities. This approach possesses a notable advantage over monoclonal antibodies (mAbs) due to its isotype-independent recruitment of immunoglobulin (Ig), which can induce Antibody-Dependent Cellular Cytotoxicity/Phagocytosis (ADCC/ADCP) via a diverse range of Fc receptor interactions.

We further demonstrated through in vitro assays that both E11-mKappa and E11-hKappa fusions can activate CDC at nanomolar concentrations and without any off-target cytotoxic effects. The high potency of these fusions at low concentrations may allow for more efficient use and potentially lower required dosages for effective treatment.

Our ongoing work on solving the crystal structure of the E11-RBD complex should provide insights on identifying the precise location of the interactions and the conserved regions on the RBD that could be targeted to develop of future therapies. Ongoing studies with PET imaging will allow us to better understand the localization and distribution in vivo and gain insights into the mechanisms of action and resistances. As a future prospect, we next aim to test the efficacy of these fusions *in vivo* with SARS-CoV-2 virus-infected mice.

Our findings suggest that E11-based nanobody fusions can be a promising therapeutic approach against COVID-19, especially in the context of emerging variants. Furthermore, this approach can be extended to eliminate any cell population that can be selectively targeted *in-vivo* by a suitable binder for a surface-exposed component, fused to a nanobody that recognizes immunoglobulin light chains. Hence this "design and delivery strategy" can be used for several protein families and can be extended to many other diseases.

References

1. Hajizadeh, F. *et al.* SARS-COV-2 RBD (Receptor binding domain) mutations and variants (A sectional-analytical study). *Microb. Pathog.* **168**, 105595 (2022).

2. Hacisuleyman, E. *et al.* Vaccine Breakthrough Infections with SARS-CoV-2 Variants. *N. Engl. J. Med.* **384**, 2212–2218 (2021).

3. Kuhlmann, C. *et al.* Breakthrough infections with SARS-CoV-2 omicron despite mRNA vaccine booster dose. *Lancet* **399**, 625–626 (2022).

4. Kared, H. *et al.* Immune responses in Omicron SARS-CoV-2 breakthrough infection in vaccinated adults. *Nat. Commun.* **13**, 4165 (2022).

5. Earnest, R. *et al.* Comparative transmissibility of SARS-CoV-2 variants Delta and Alpha in New England, USA. *Cell Reports Med.* **3**, 100583 (2022).

6. Bálint, G., Vörös-Horváth, B. & Széchenyi, A. Omicron: increased transmissibility and decreased pathogenicity. *Signal Transduct. Target. Ther.* **7**, 151 (2022).

7. Mengist, H. M., Kombe Kombe, J. A. & Jin, T. Immune Evasion by the Highly Mutated SARS-CoV-2 Omicron Variant. *Infect. Drug Resist.* **Volume 15**, 4013–4027 (2022).

8. Takashita, E. *et al.* Efficacy of Antiviral Agents against the SARS-CoV-2 Omicron Subvariant BA.2. *N. Engl. J. Med.* **386**, 1475–1477 (2022).

9. Cully, M. A tale of two antiviral targets — and the COVID-19 drugs that bind them. *Nat. Rev. Drug Discov.* **21**, 3–5 (2022).

10. Focosi, D. *et al.* Monoclonal antibody therapies against SARS-CoV-2. *Lancet Infect. Dis.* **22**, e311–e326 (2022).

11. Dougan, M. *et al.* Bamlanivimab plus Etesevimab in Mild or Moderate Covid-19. *N. Engl. J. Med.* **385**, 1382–1392 (2021).

12. Taylor, P. C. *et al.* Neutralizing monoclonal antibodies for treatment of COVID-19. *Nat. Rev. Immunol.* **21**, 382–393 (2021).

13. Fiaschi, L. *et al.* Efficacy of Licensed Monoclonal Antibodies and Antiviral Agents against the SARS-CoV-2 Omicron Sublineages BA.1 and BA.2. *Viruses* **14**, 1374 (2022).

14. https://www.idsociety.org/covid-19-real-time-learning-network/therapeutics-and-interventions/monoclonal-antibodies/.

15. Casadevall, A. Passive Antibody Therapies: Progress and Continuing Challenges. *Clin. Immunol.* **93**, 5–15 (1999).

16. Lipschultz, C. A., Yee, A., Mohan, S., Li, Y. & Smith-Gill, S. J. Temperature differentially affects encounter and docking thermodynamics of antibody-antigen association. *J. Mol. Recognit.* **15**, 44–52 (2002).

17. Lin, C.-Y. & Liu, J. C. Modular protein domains: an engineering approach toward functional biomaterials. *Curr. Opin. Biotechnol.* **40**, 56–63 (2016).

18. Muyldermans, S. Nanobodies: Natural Single-Domain Antibodies. *Annu. Rev. Biochem.* **82**, 775–797 (2013).

19. Dolk, E. *et al.* Isolation of Llama Antibody Fragments for Prevention of Dandruff by Phage Display in Shampoo. *Appl. Environ. Microbiol.* **71**, 442–450 (2005).

20. Ingram, J. R., Schmidt, F. I. & Ploegh, H. L. Exploiting Nanobodies' Singular Traits. *Annu. Rev. Immunol.* **36**, 695–715 (2018).

21. Wesolowski, J. *et al.* Single domain antibodies: promising experimental and therapeutic tools in infection and immunity. *Med. Microbiol. Immunol.* **198**, 157–174 (2009).

22. Harmsen, M. M. & De Haard, H. J. Properties, production, and applications of camelid single-domain antibody fragments. *Appl. Microbiol. Biotechnol.* **77**, 13–22 (2007).

23. Cheloha, R. W., Harmand, T. J., Wijne, C., Schwartz, T. U. & Ploegh, H. L. Exploring cellular biochemistry with nanobodies. *J. Biol. Chem.* **295**, 15307–15327 (2020).

24. Bradbury, A. & Plückthun, A. Reproducibility: Standardize antibodies used in research. *Nature* **518**, 27–29 (2015).

25. Van holsbeeck, K., Martins, J. C. & Ballet, S. Downsizing antibodies: Towards complementarity-determining region (CDR)-based peptide mimetics. *Bioorg. Chem.* **119**, 105563 (2022).

26. Schütz, D. *et al.* Peptide and peptide-based inhibitors of SARS-CoV-2 entry. *Adv. Drug Deliv. Rev.* **167**, 47–65 (2020).

27. Wójcik, P. & Berlicki, Ł. Peptide-based inhibitors of protein–protein interactions. *Bioorg. Med. Chem. Lett.* **26**, 707–713 (2016).

28. Schymkowitz, J. *et al.* The FoldX web server: an online force field. *Nucleic Acids Res.* **33**, W382–W388 (2005).

29. Roy, A. A., Dhawanjewar, A. S., Sharma, P., Singh, G. & Madhusudhan, M. S. Protein Interaction Z Score Assessment (PIZSA): an empirical scoring scheme for evaluation of protein–protein interactions. *Nucleic Acids Res.* **47**, W331–W337 (2019).

30. Hanke, L. *et al.* Multivariate mining of an alpaca immune repertoire identifies potent cross-neutralizing SARS-CoV-2 nanobodies. *Sci. Adv.* **8**, (2022).

31. Hajizadeh, F. *et al.* SARS-COV-2 RBD (Receptor binding domain) mutations and variants (A sectional-analytical study). *Microb. Pathog.* **168**, 105595 (2022).

32. Premkumar, L. *et al.* The receptor-binding domain of the viral spike protein is an immunodominant and highly specific target of antibodies in SARS-CoV-2 patients. *Sci. Immunol.* **5**, (2020).

33. da Costa, C. H. S., de Freitas, C. A. B., Alves, C. N. & Lameira, J. Assessment of mutations on RBD in the Spike protein of SARS-CoV-2 Alpha, Delta and Omicron variants. *Sci. Rep.* **12**, 8540 (2022).

34. Vincke, C. *et al.* Generation of Single Domain Antibody Fragments Derived from Camelids and Generation of Manifold Constructs. in 145–176 (2012). doi:10.1007/978-1-61779-974-7_8.

35. Arbabi-Ghahroudi, M. Camelid Single-Domain Antibodies: Historical Perspective and Future Outlook. *Front. Immunol.* **8**, (2017).

36. Kim, E. & Koo, H. Biomedical applications of copper-free click chemistry: in vitro , in vivo , and ex vivo. *Chem. Sci.* **10**, 7835–7851 (2019).

37. Sletten, E. M. & Bertozzi, C. R. Bioorthogonal Chemistry: Fishing for Selectivity in a Sea of Functionality. *Angew. Chemie Int. Ed.* **48**, 6974–6998 (2009).

38. Popp, M. W., Antos, J. M., Grotenbreg, G. M., Spooner, E. & Ploegh, H. L. Sortagging: a versatile method for protein labeling. *Nat. Chem. Biol.* **3**, 707–708 (2007).

39. Ritzefeld, M. Sortagging: A Robust and Efficient Chemoenzymatic Ligation Strategy. *Chem. - A Eur. J.* **20**, 8516–8529 (2014).

40. Ali, I., Aboul-Enein, H. Y., Singh, P., Singh, R. & Sharma, B. Separation of biological proteins by liquid chromatography. *Saudi Pharm. J.* **18**, 59–73 (2010).

41. Zhang, G., Pomplun, S., Loftis, A. R., Loas, A. & Pentelute, B. L. The first-in-class peptide binder to the SARS-CoV-2 spike protein. *bioRxiv* 2020.03.19.999318 (2020) doi:10.1101/2020.03.19.999318.

42. Pomplun, S. *et al.* De Novo Discovery of High-Affinity Peptide Binders for the SARS-CoV-2 Spike Protein. *ACS Cent. Sci.* **7**, 156–163 (2021).

43. Hulme, E. C. & Trevethick, M. A. Ligand binding assays at equilibrium: validation and interpretation. *Br. J. Pharmacol.* **161**, 1219–1237 (2010).

44. Merle, N. S., Church, S. E., Fremeaux-Bacchi, V. & Roumenina, L. T. Complement System Part I â€“ Molecular Mechanisms of Activation and Regulation. *Front. Immunol.* **6**, (2015).

45. Ricklin, D., Hajishengallis, G., Yang, K. & Lambris, J. D. Complement: a key system for immune surveillance and homeostasis. *Nat. Immunol.* **11**, 785–797 (2010).

46. Walport, M. J. Complement. *N. Engl. J. Med.* **344**, 1058–1066 (2001).

47. Lambris, J. D., Ricklin, D. & Geisbrecht, B. V. Complement evasion by human pathogens. *Nat. Rev. Microbiol.* **6**, 132–142 (2008).

48. Meyer, S., Leusen, J. H. & Boross, P. Regulation of complement and modulation of its activity in monoclonal antibody therapy of cancer. *MAbs* **6**, 1133–1144 (2014).

49. Nimmerjahn, F. & Ravetch, J. V. Fcγ receptors as regulators of immune responses. *Nat. Rev. Immunol.* **8**, 34–47 (2008).

50. Natsume, A. *et al.* Engineered Antibodies of IgG1/IgG3 Mixed Isotype with Enhanced Cytotoxic Activities. *Cancer Res.* **68**, 3863–3872 (2008).

51. Bruhns, P. Properties of mouse and human IgG receptors and their contribution to disease models. *Blood* **119**, 5640–5649 (2012).

52. Aicheler, R., Wang, E., Tomasec, P., Wilkinson, G. & Stanton, R. Potential for Natural Killer Cell-Mediated Antibody-Dependent Cellular Cytotoxicity for Control of Human Cytomegalovirus. *Antibodies* **2**, 617–635 (2013).

53. Rosenbaum, D. M., Rasmussen, S. G. F. & Kobilka, B. K. The structure and function of G-protein-coupled receptors. *Nature* **459**, 356–363 (2009).

54. McPherson, A. Chapter 1 Introduction to the Crystallization of Biological Macromolecules. in 5–23 (2009). doi:10.1016/S1063-5823(09)63001-5.

55. D'Arcy, A., Bergfors, T., Cowan-Jacob, S. W. & Marsh, M. Microseed matrix screening for optimization in protein crystallization: what have we learned? *Acta Crystallogr. Sect. F Struct. Biol. Commun.* **70**, 1117–1126 (2014).

56. Alauddin, M. M. Positron emission tomography (PET) imaging with (18)F-based radiotracers. *Am. J. Nucl. Med. Mol. Imaging* **2**, 55–76 (2012).

57. Cheng, Z., Al Zaki, A., Hui, J. Z., Muzykantov, V. R. & Tsourkas, A. Multifunctional nanoparticles: cost versus benefit of adding targeting and imaging capabilities. *Science* **338**, 903–10 (2012).

58. Webb, B. & Sali, A. Comparative Protein Structure Modeling Using MODELLER. *Curr. Protoc. Bioinforma.* **54**, (2016).

59. Buß, O., Rudat, J. & Ochsenreither, K. FoldX as Protein Engineering Tool: Better Than Random Based Approaches? *Comput. Struct. Biotechnol. J.* **16**, 25–33 (2018).

60. Berendsen, H. J. C., van der Spoel, D. & van Drunen, R. GROMACS: A message-passing parallel molecular dynamics implementation. *Comput. Phys. Commun.* **91**, 43–56 (1995).

61. Bjelkmar, P., Larsson, P., Cuendet, M. A., Hess, B. & Lindahl, E. Implementation of the CHARMM Force Field in GROMACS: Analysis of Protein Stability Effects from Correction Maps, Virtual Interaction Sites, and Water Models. *J. Chem. Theory Comput.* **6**, 459–466 (2010).

Appendix

Supplementary Tables

Peptide	**FoldX $\Delta G_{binding}$ (kcal mol^{-1})**	**PIZSA Z -score**	**Sequence**	**Binding Location**
ACE2-derived peptide	-9.97	2.601	QAKTFLDKFNHEAEDLF YQSSL	**417, 446**, 447, 449, 453, 455, 456, 473, 475, 476, **484, 486, 487, 489, 493, 496, 498,** 500, **501**, 502, **505**
7ls9_C_E_3867	-12.93	3.153	HRWAYCINGVCFGAY	**346**, 351, **444**, 445**, 446**, 447, 448, 449, 450, **452**, 470, **490**, 492, **493**, 494
6xkp_B_M_919	-12.13	3.279	RGSSGWYRIGTRWGNW	356, 347, 349, 351, **444**, 445, **446**, 447, 448, 449, 450, 451, **452**, 470, **484**, **490**, 492, **493, 494**, **498**
7kn5_B_D_619	-11.11	3.083	VGTYYSGNYHYTCSDD	351, **417,** 449, 450, **452**, 455, 456, 468, 470, **484,** 486, **489**, **490,** 492, **493, 494**, 495, **496**
7m7w_S_C_752	-11.17	2.884	WSHYTYDYY	355, 396, 426, 428, 429, 430, 463, 464, 514, 515, 516, 518, 519, 520
7kmg_C_A_47	-10.36	2.973	WMGRIIPILGIAN	351, 449, 450, **452**, 470, 472, 481, 482, 483, **484**, **490**, 492
7l0n_R_A_312	-10.18	2.340	YTRGAWFGESLI	334, 335, 336, 337, **339**, 340, 341, 343, 344, 345, **346,** 354,356, 357, 358, 359, 360, 361, 441, 509
Mutation Hotspot Residues: 339, 346, 371, 373, 375, 376, 405, 408, 417, 439, 440, 444, 446, 452, 460, 477, 478, 484, 486, 489, 490, 493, 494, 496, 498, 501, 505				

Table S1. Summary of shortlisted peptide candidates, including sequence, target location, FOLDX binding energies, and PIZSA Z-scores. Residue locations that overlapped between peptide binding location and the mutation hotspot are highlighted in bold.

VHH	Conjugate partner	Purpose
E11	GGG-Rhodamine	Size Exclusion Chromatography (SEC)
E11	GGG- Biotin	ELISA
E11	GGG-Azide	Synthesis of chemical fusion with hKappa VHH
E11	GGG-NOTA-Azide	Synthesis of E11-NOTA-Azide-DBCO-$(PEG)_{20}$ compound PET imaging studies
hKappa VHH	GGG-DBCO	Synthesis of chemical fusion with E11-azide

Table S2. **Summary of nanobody labelling using sortagging reaction**: The table provides a list of different nanobodies that were conjugated using the sortagging reaction, along with the type of substrate used and their applications.

Treatment	Effector cells	Incubation time	Effector to target cell ratio	Additional comments
E11-mKappa (GF) + mouse IgG	BMD-NK cells	16h	1:1	A wash step was included before addition of the CellTiter-Glo buffer to wash of any BMD-NK cells.
E11-mKappa (GF) + mouse IgG	Unfractionated spleenocytes	12h	1:10	No wash step was included.
E11-hKappa (CF) + human IgG	ADCC Bioassay reporter Cells	6h	1:5-10	Protocol prescribed by Promega's ADCC Reporter Bioassay kit was followed.

Table S3. **ADCC treatment conditions**. The table presents the different treatment conditions tested to determine the optimal conditions for Antibody dependent cellular cytotoxicity (ADCC), along with the effector cells used, incubation time, and target to effector cell ratio.

Supplementary Figures

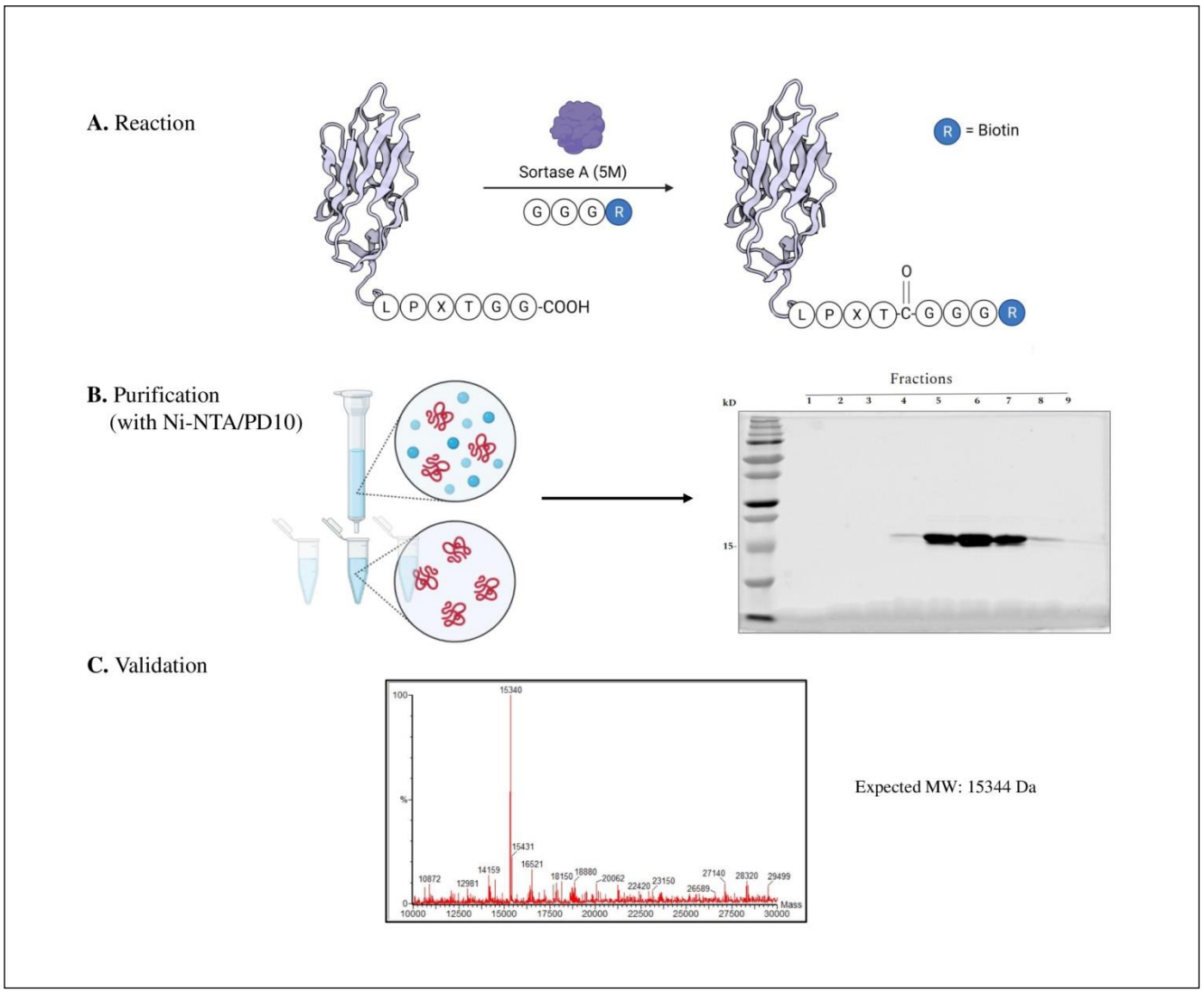

Figure S1. Sotagging procedure. (A) Schematic representation of the sortagging reaction between the LPXTGG tagged nanobody and GGG-Biotin, resulting in the biotinylated nanobody. (B) Purification of unreacted substrate using Ni-NTA/PD10 to remove unreacted nanobody containing 6XHis. (C) Verification of the final conjugated product using LCMS. The graph shows the mass spectra of the biotinylated nanobody, with the expected mass peak at 15,344 Da.

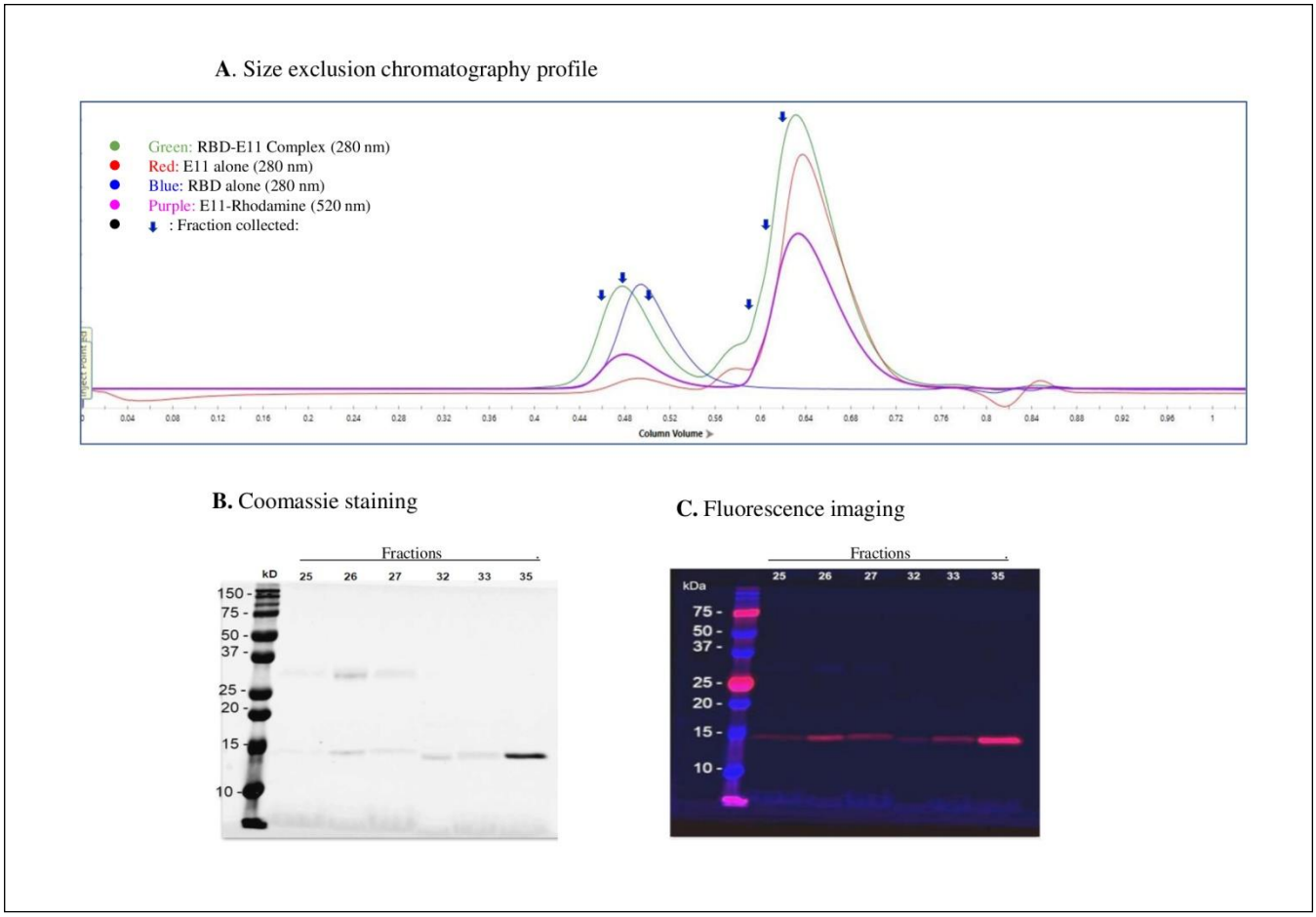

Figure S2. SEC-based binding study of E11. (A) Elution profiles of RBD-E11 complex (green), E11 (red), and RBD (blue. The rhodamine emission wavelength is depicted in purple, and a shift in the peak is observed for the RBD-E11 complex. (B) Coomassie staining and (C) Rhodamine blot of peak fractions collected from the FPLC run of E11-Rh-RBD complex. The figure shows the SEC-based binding study of E11 and RBD, where the RBD-E11 complex eluted at a different retention time compared to E11 or RBD alone. The Coomassie staining and fluorescence imaging of peak fractions confirms the presence of RBD and E11 in the eluted fractions.

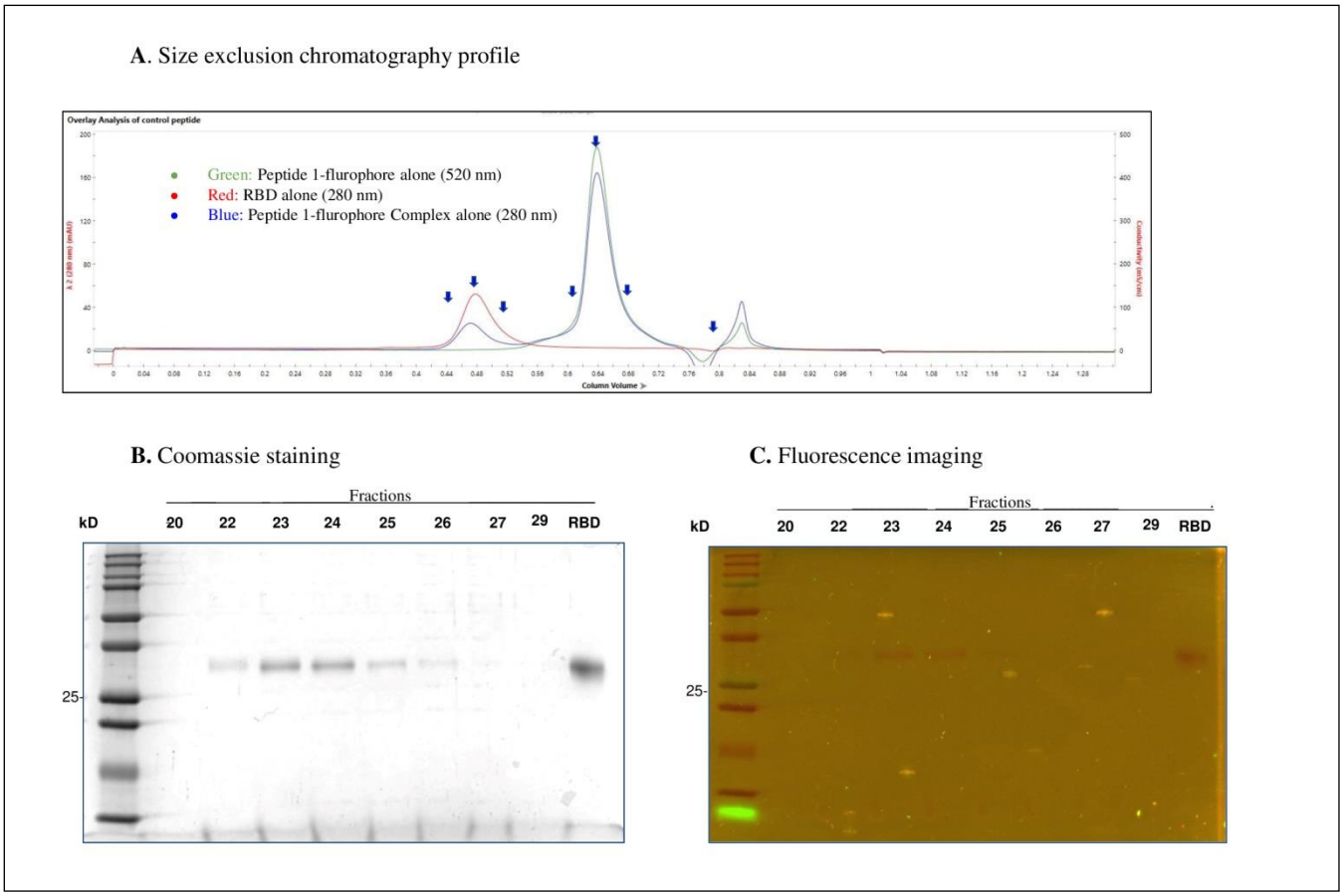

Figure S3. SEC-based binding study of Peptide 1 (6xkp_B_M_919). (A) Elution profiles of RBD-Peptide-1-complex (green), RBD (red), and Peptide-1 (blue) (B) Coomassie staining and (C) fluorescence imaging of peak fractions collected from the FPLC run of Peptide-1-RBD complex.

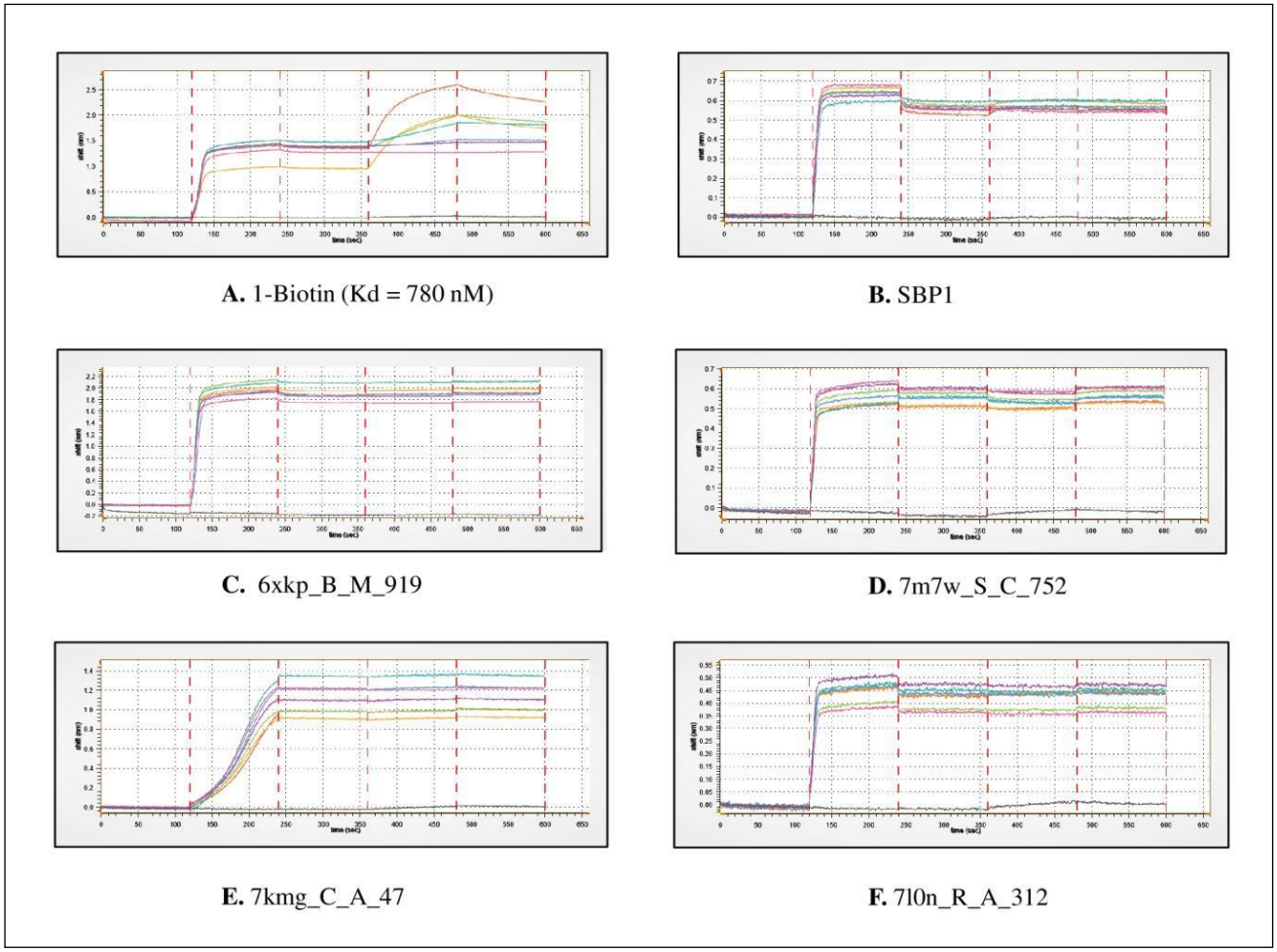

Figure S4. BLI based binding study. BLI curves for the association and dissociation of Biotin-1, SBP1, 6xkp_B_M_919, 7m7w_S_C_752, 7kmg_C_A_47, and 7l0n_R_A_312 peptides, shown in panels (A)-(F), to the spike-RBD. Among the tested peptides, only Biotin-1 exhibited nanomolar affinity while the others failed to bind within the range of tested concentrations (250 nM-8 µM).

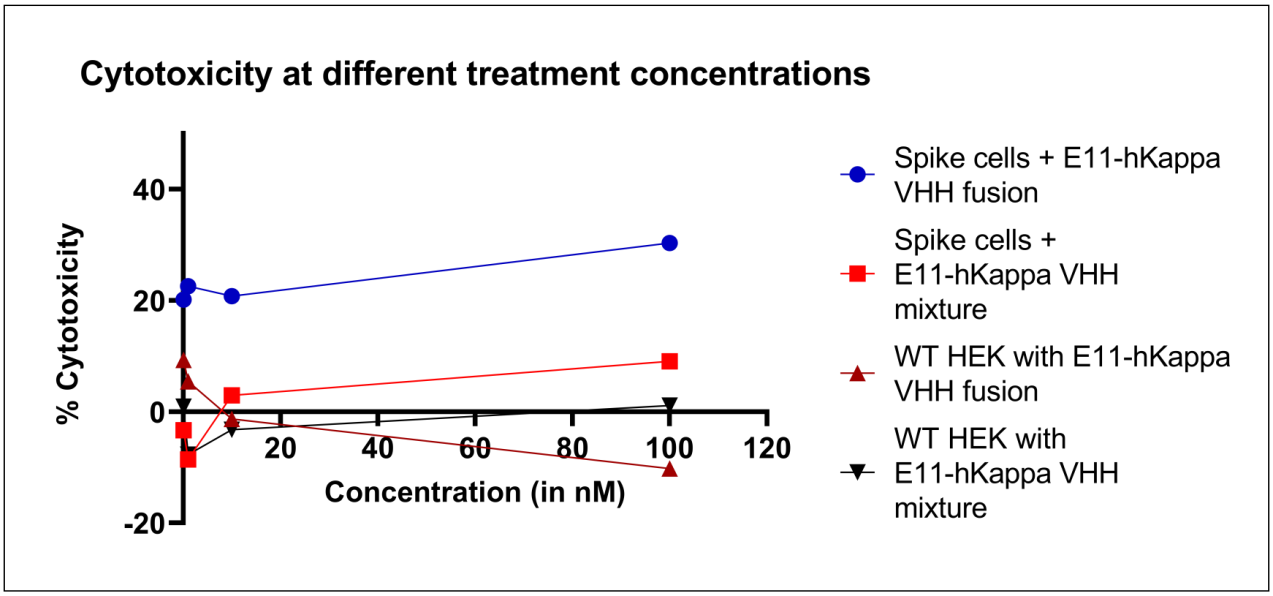

Figure S5.Activation of CDC at different nanomolar concentrations. The percentage of cytotoxicity was evaluated for different groups at different concentrations - 0.1 nM, 1 nM, 10 nM, and 100 nM. Only spike expressing HEK293 cells treated with E11-hKappa VHH (CF) showed high levels of cytotoxicity for all four treatment concentrations, indicating the effectiveness of the treatment.

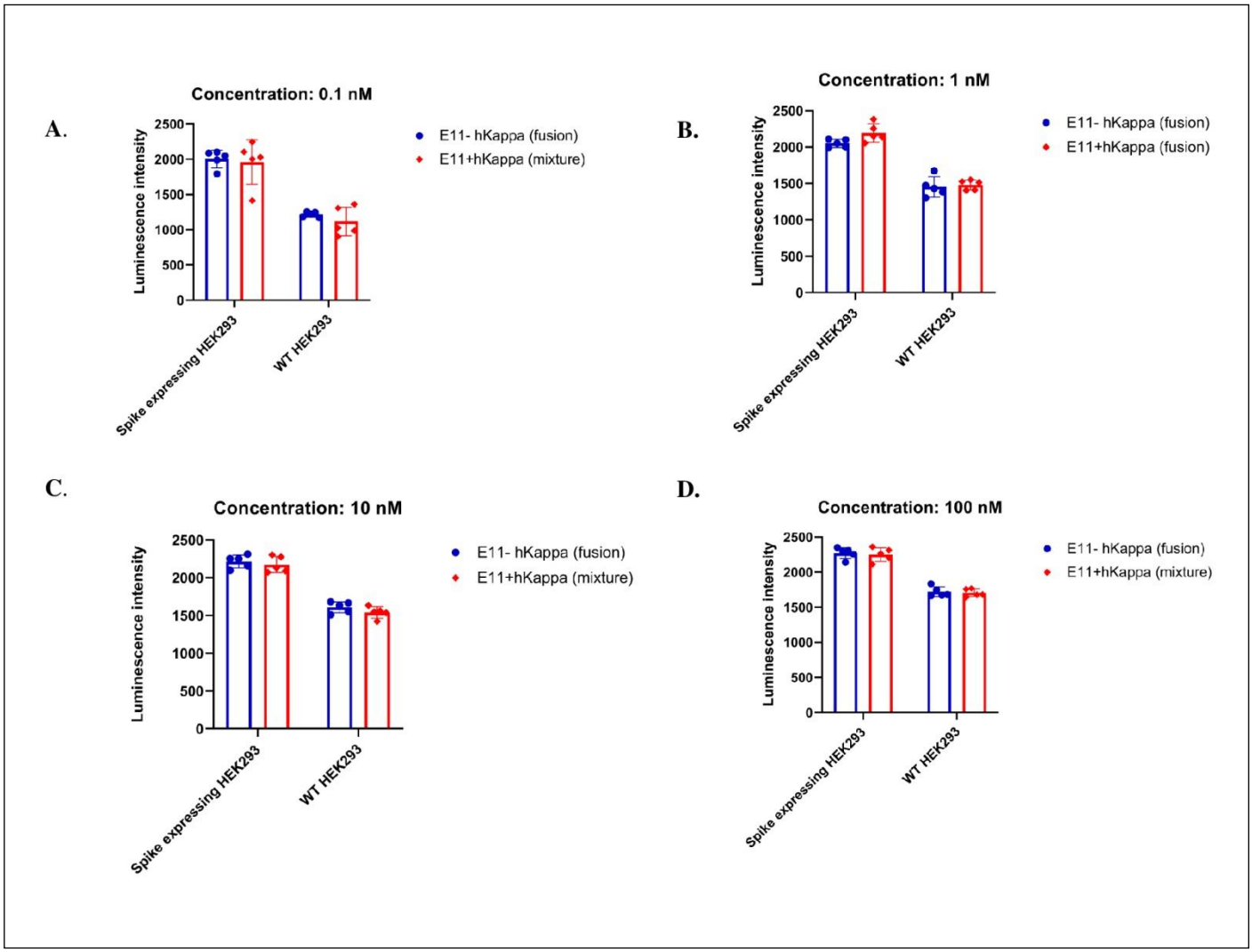

Figure S6.ADCC with ADCC bioassay reporter cells (Promega). Spike expressing HEK293 cells induced expression of luciferase in reporter cells that express luciferase upon engagement of mouse FcγRIV receptor in the presence of E11-mKappa VHH (CF) and mouse polyclonal mouse IgG. E11-mKappa fusion and mixture treatments were tested at 4 different concentrations of 0.1 nM, 1 nM, 10 nM, and 100 nM, as depicted in panels (A)-(D). Differences in luminescence intensity between the fusion-treated groups and individual component mixture-treated group were analyzed by t test (n = 5). No significant difference was observed.

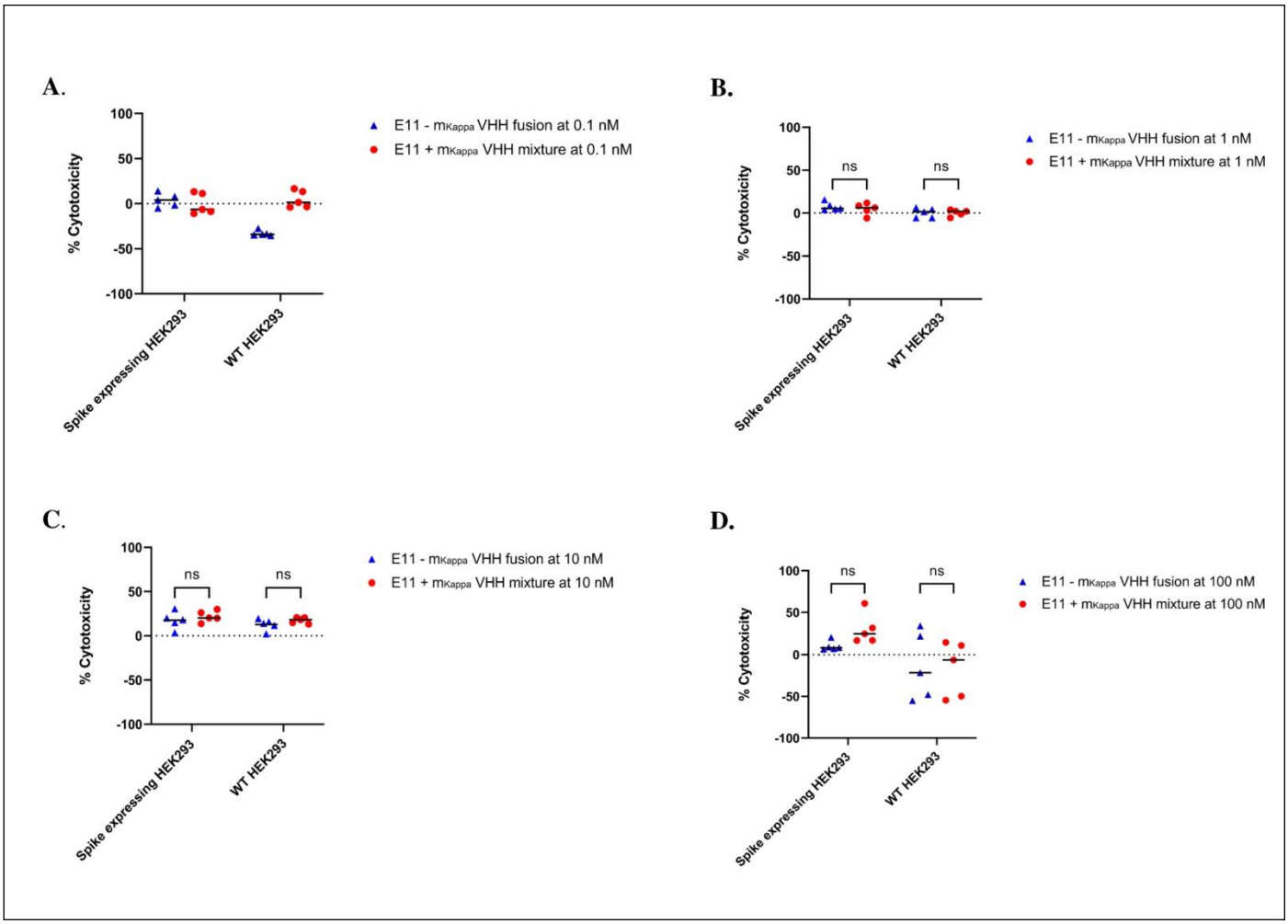

Figure S7. ADCC with unfractionated spleenocytes. Spike-expressing HEK293 cells and control HEK293 cells were exposed to treatment groups consisting of E11-mKappa VHH (CF) and a mixture of its individual components at four different concentrations (0.1 nM, 1 nM, 10 nM, and 100 nM), as depicted in panels (A)-(D). After a 12-hour incubation period with unfractionated spleenocytes, no significant difference in %cytotoxicity was observed between the fusion-treated and mixture-treated groups. The % cytotoxicity for the fusion-treated groups and the group treated with the individual components as a mixture were analyzed using a t-test (n = 5).

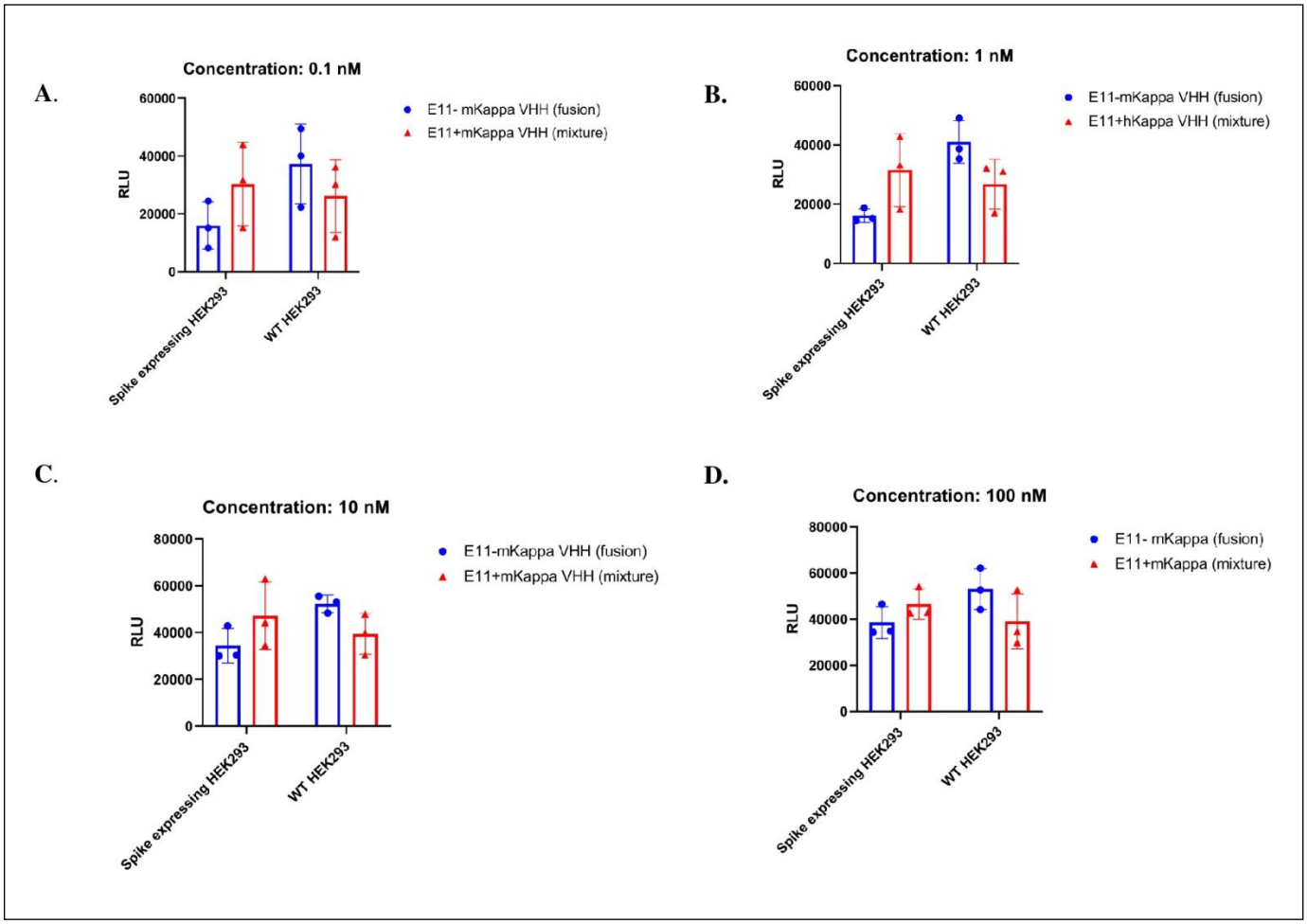

Figure S8. ADCC with BMD-NK cells. Spike-expressing HEK293 cells and control HEK293 cells were exposed to treatment groups consisting of E11-mKappa VHH (CF) and a mixture of its individual components at 4 different concentrations of 0.1 nM, 1 nM, 10 nM and 100 nM, as depicted in panels (A)-(D). After a 16-hour incubation period with BMD-NK cells, there was some difference observed between the fusion-treated and mixture-treated groups. However, the difference of % cytotoxicity for the fusion-treated groups and the group treated with the individual components as a mixture was not found to be statistically significant when analysed using a Student's t-test (n=5).

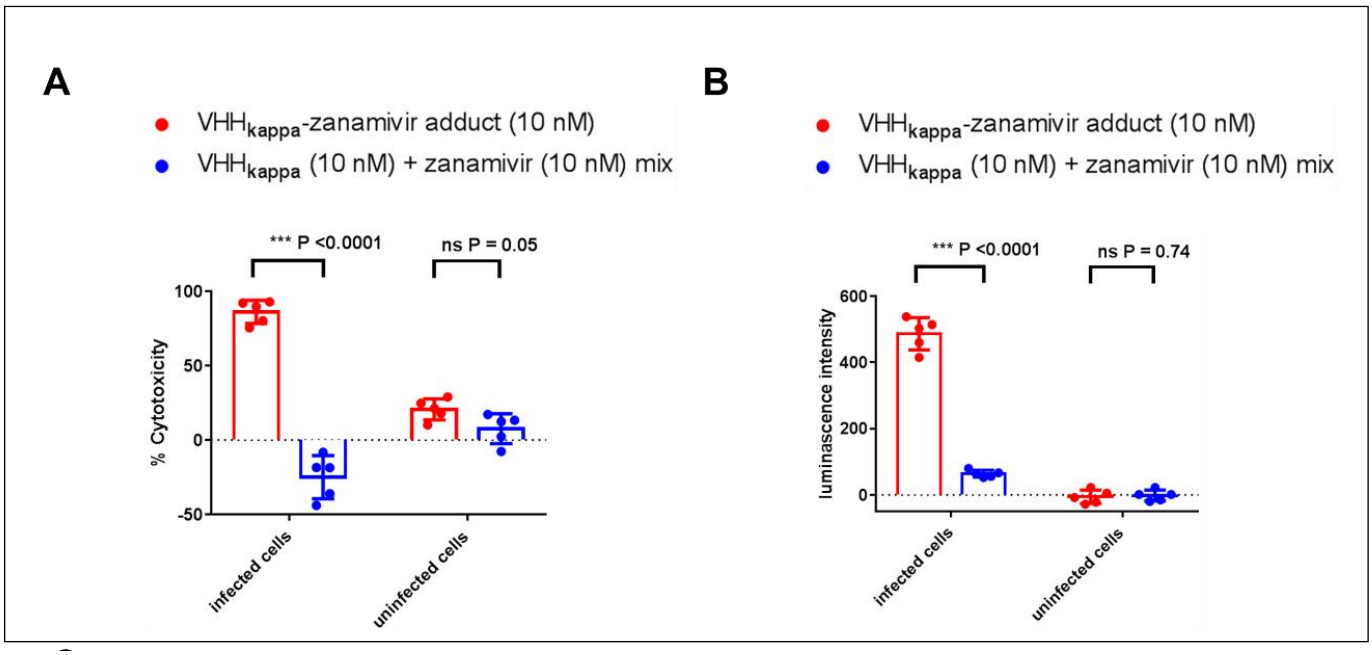

Figure S9. Zanamvir-mKappa VHH induces CDC and ADCC. (A) Influenza virus-infected MDCK cells were killed by zanamivir-mKappa VHH (CF) in the presence of rabbit complement and mouse polyclonal mouse IgG. Differences in the % cytotoxicity for the zanamivir-mKappa VHH (CF) treated groups and the group treated with the individual components as a mixture were analyzed by t-test (n = 5). (**B**) Virus-infected MDCK cells induced expression of luciferase in reporter cells that express luciferase upon engagement of mouse FcγRIV receptor in the presence of zanamivir-mKappa VHH and mouse polyclonal mouse IgG. Differences in luminescence intensity between the fusion-treated groups and individual component mixture-treated group were analyzed by t test (n = 5) (Courtesy: Xin Liu).

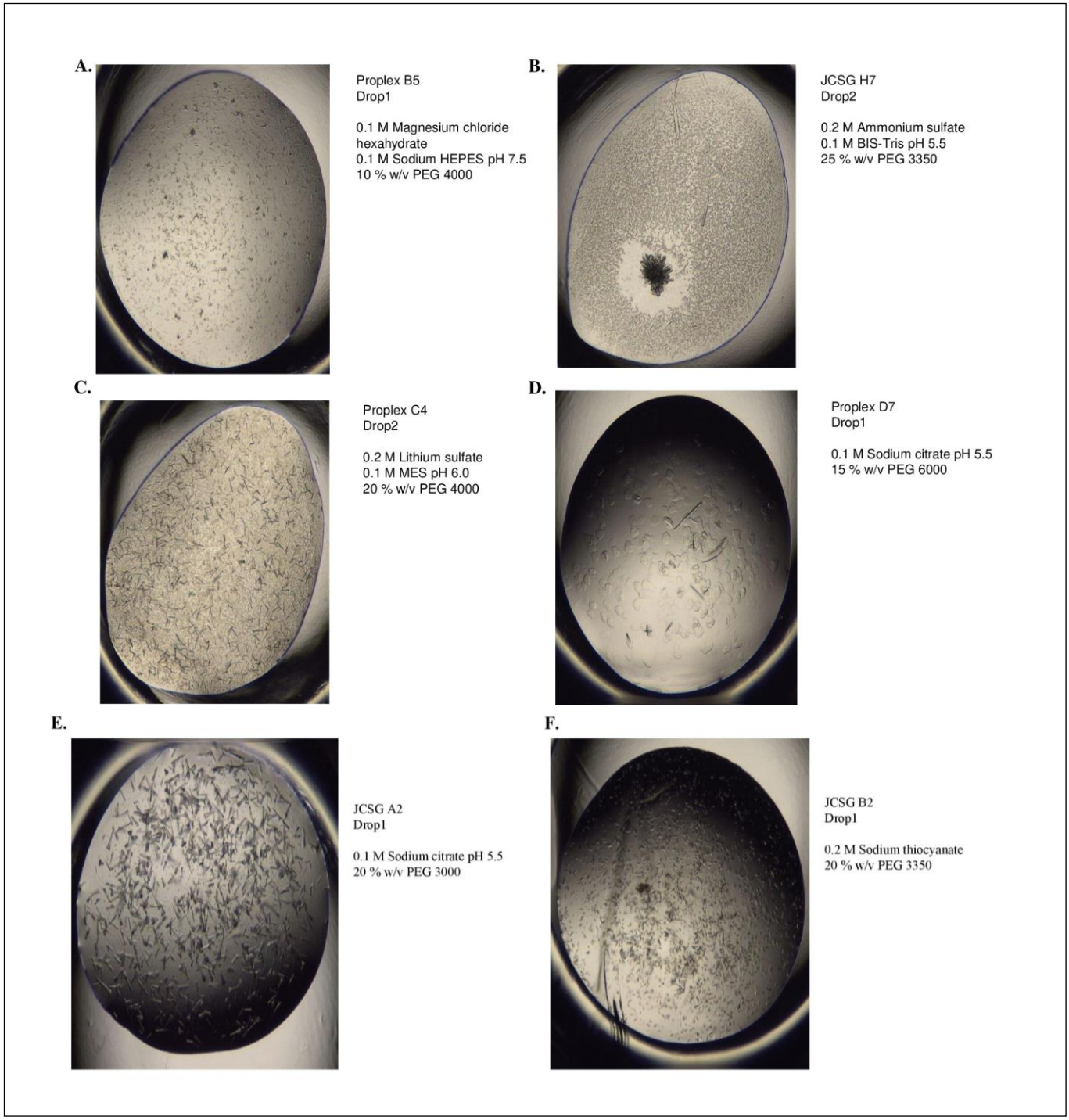

Figure S10. Observation of rod and needle-shaped crystals in droplets. Microcrystallization experiments were performed using an Art Robbins Phoenix micropipetting robot at MIT. The images (A)-(F) depict crystals formed under six distinct conditions. The crystals appear as elongated rods and needles, indicating the presence of specific growth planes in the crystal lattice.

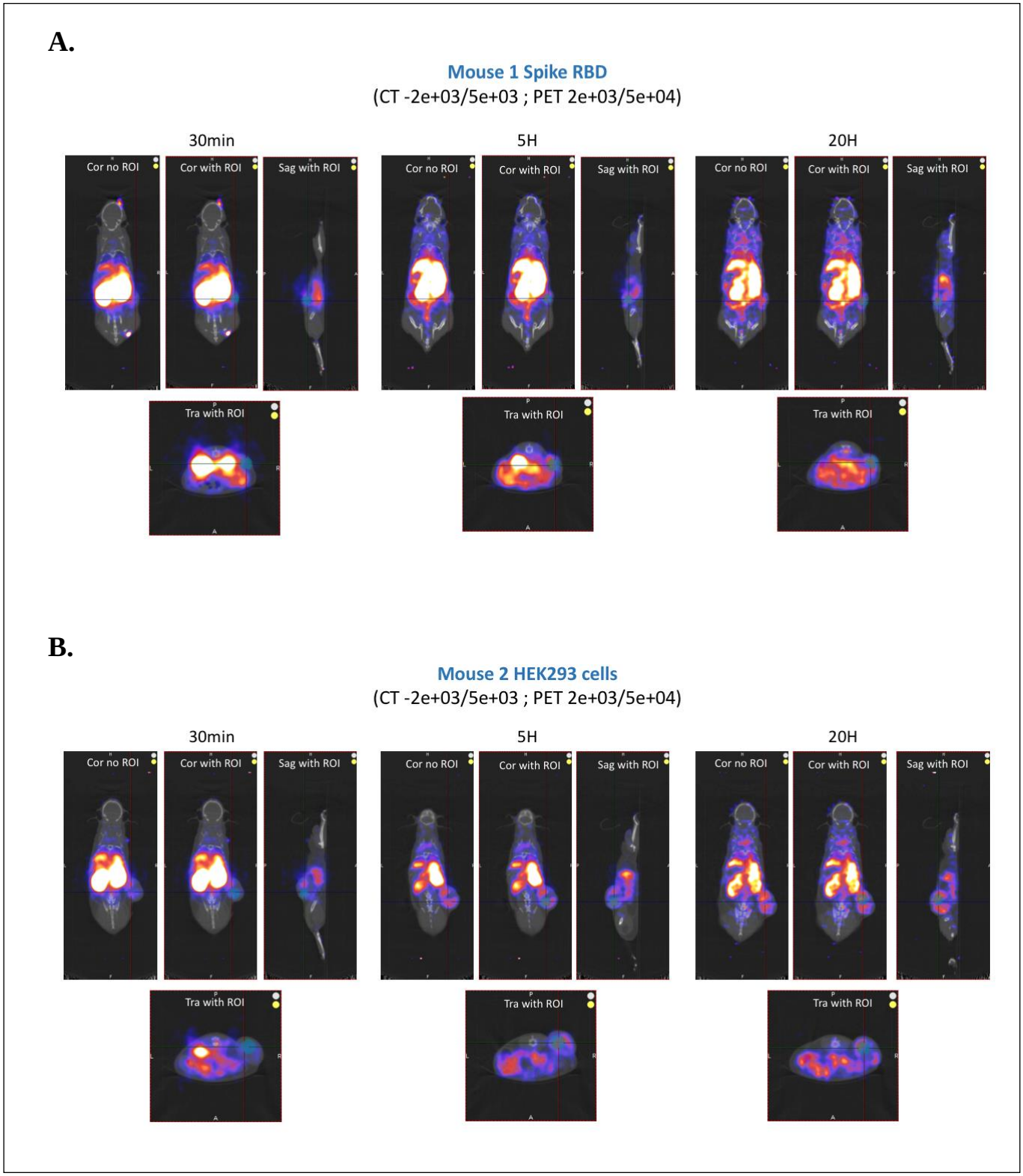

Figure S11. PET imaging of Spike expressing-HEK293 and WT-HEK293 tumours using 64Cu-E11-PEG20-NOTA *in vivo*. Tumour-bearing mice were imaged 1, 5, and 20 h after administration of 100 µCi of 64Cu-E11-PEG20-NOTA (n = 3). Colour intensity optimization was performed to visualize the tumours clearly with and without ROI measurements on the PET/CT image.

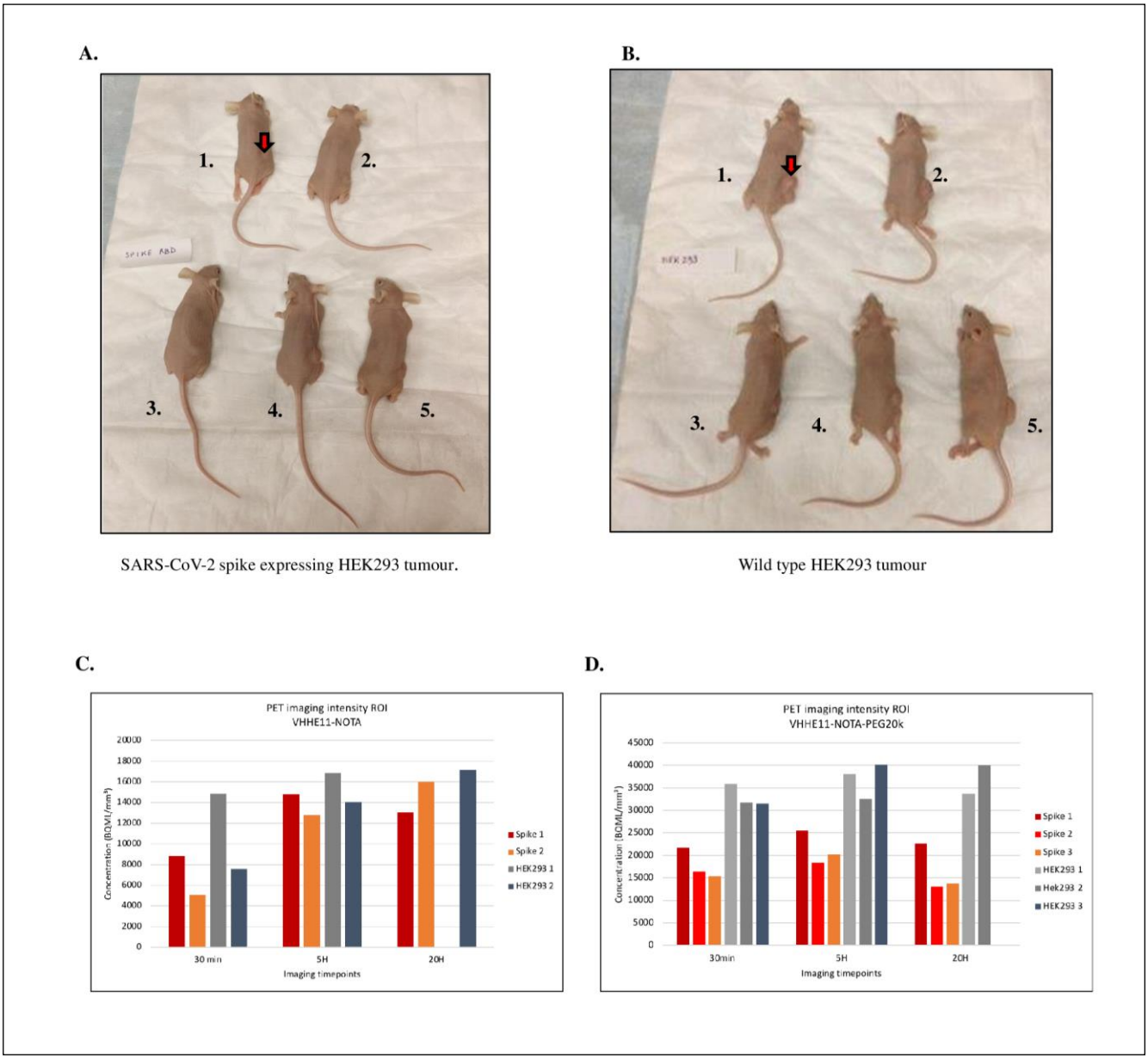

Figure S12. Tumour sizes and PET imaging intensity measurements (ROI). Tumour size comparison between mice grafted with (A) Spike expressing HEK293 cells and (B) WT-HEK293 cells. ROI intensity measurements of both groups of mice injected with 100 μCi of 64Cu-E11-NOTA (C) and (D) 64Cu-E11-PEG20-NOTA at 30 min, 5h and 20h time points.

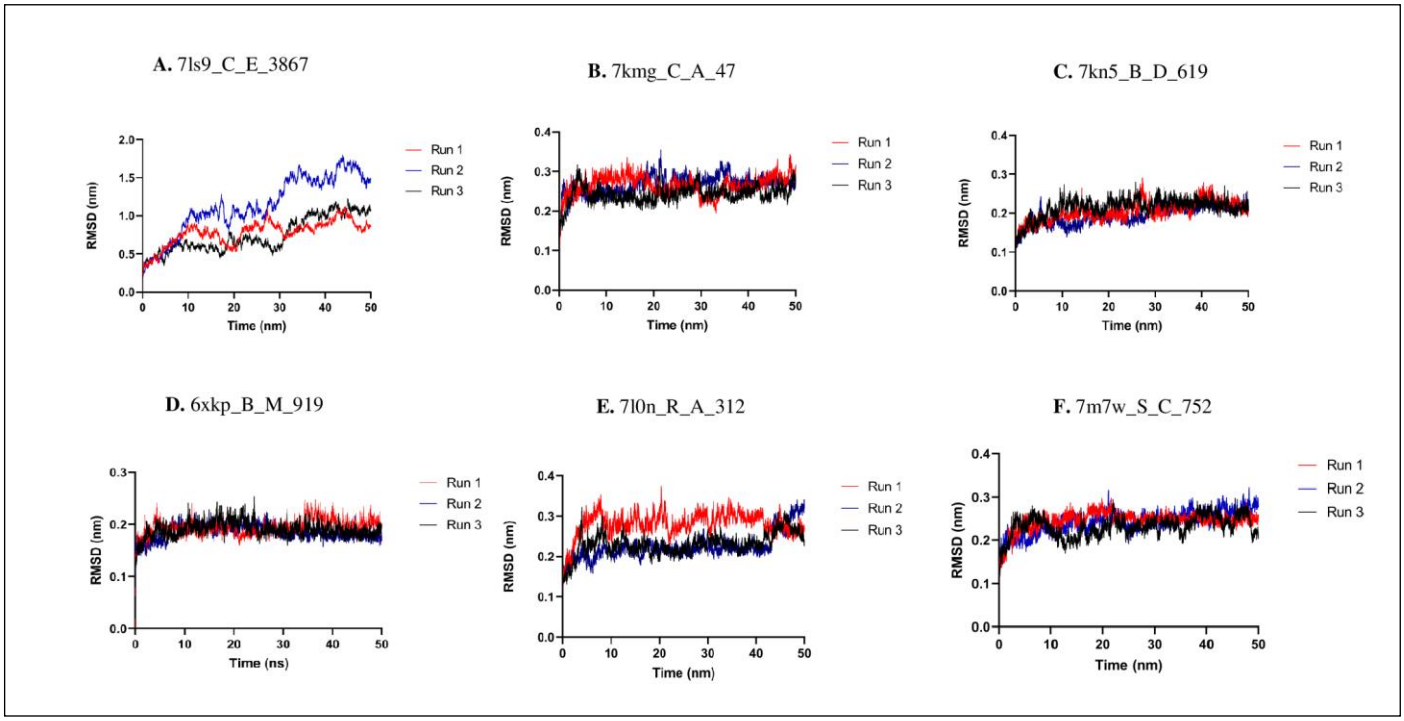

Figure S13: Root mean square deviation (RMSD) analysis of RBD-peptide complexes. The RMSD plots were generated to validate the conformational stability of RBD-peptide complexes in three independent molecular dynamics (MD) runs. RMSD plotted against time for the six shortlisted peptide candidates, including 7ls9_C_E_38767, 7kmg_C_A_47, 7kn5_B_D_619, 6xkp_B_M_919, 7l0n_R_A_312 and 7m7w_S_C_752, in panels (A)-(F) respectively.

A.

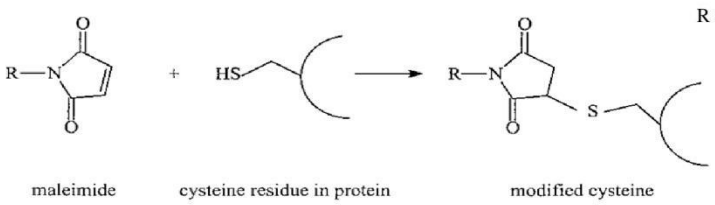

B.

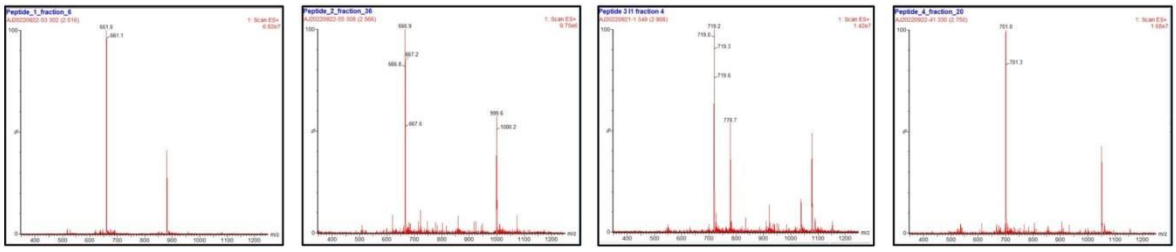

C.

Peptide name	MW	Product weight	M/2	M/3	M/4
6xkp_B_M_919	2042.26	2639.26	1319.63	879.7533333	**659.815**
7m7w_S_C_752	1400	1997	998.5	**665.6666667**	499.25
7kmg_C_A_47	1556.95	2153.95	1076.975	**717.9833333**	538.4875
7l0n_R_A_312	1502	2099	1049.5	**699.6666667**	524.75

Figure S14. Synthesis of biotinylated peptides. (A) Scheme of the thiol-maleimide reaction between cysteine and Biotin-PEG-maleimide, showing the formation of a biotin conjugated product. (B) LCMS spectra of the reaction product, highlighting the peak corresponding to the biotinylated peptide. (C) Theoretical M/Z ratios of the reaction product for LCMS confirmations, showing good agreement with the observed ratios. The successful biotinylation of the peptide is confirmed by the presence of the highlighted peak in the LCMS spectra.